Top-contact Lateral Organic Photodetectors for Deep Ultraviolet Applications

by

Thomas Borel

A thesis

presented to the University of Waterloo

in fulfillment of the

thesis requirement for the degree of

Master of Applied Science

in

Electrical and Computer Engineering -Nanotechnology

Waterloo, Ontario, Canada, 2013

Author's Declaration

I hereby declare that I am the sole author of this thesis. This is a true copy of the thesis, including any required final revisions, as accepted by my examiners.

I understand that my thesis may be made electronically available to the public.

Abstract

Organic semiconductors are very attractive for thin film Organic Photodetectors (OPDs) since they possess a number of desirable attributes for optical sensing including high absorption coefficients over visible and ultraviolet wavelengths and compatibility with large-area deposition processes such as ink-jet, screen printing, and solution processing.

OPDs, in general, utilize a vertical device architecture where the photoactive organic semiconductor layers are sandwiched between top and bottom electrodes that provide electrical contact. More recently, an interest in utilizing a lateral device architecture instead of the vertical one, has emerged. In this architecture, the two contacts are positioned on the two sides of the photoactive material with respect to the direction of the incoming signal, separated by a small gap. However, the factors governing lateral OPDs' photo-response are still not well understood.

In this thesis, we fabricate top-contact lateral OPDs using a thermal evaporation only fabrication process. We study the factors governing both the dark and photo currents of lateral OPDs. The effect of the wide gap between the two electrodes on the current-voltage characteristics is discussed and the role of space charge limited conduction is investigated. The contributions in the photoresponse of light scattering through the active layers as well as the back reflection of light at the metallic contacts are emphasized.

The reproducibility over repeated operation cycles of both dark and photo currents values is explored. Exposure to light of the lateral OPD is found to lead to a significant increase in the dark current. The role of the conductivity enhancement in the channel due to light-induced trap filling is investigated.

External quantum efficiency and detectivity estimates are given for deep ultraviolet lateral (DUV) OPDs. A comparison with vertical DUV OPDs performances is provided.

Finally, the use of a phosphorescent sensitizer doped in the absorbing bottom layer to improve top-contact lateral OPDs efficiency is discussed.

Acknowledgments

First and foremost, I would like to thank my supervisor, Professor H. Aziz, for aiding me in the completion of my thesis. Not only has he helped analyze my results, but he has also given me continuous support, encouragement and patience throughout the duration of my MASc at the University of Waterloo.

I would like to thank Professors A. Sazonov and D. Ban for taking the time and consideration to read and review my thesis.

I sincerely thank Richard Barber, technical manager of the Giga-to-Nanoelectronics Centre, and Robert Mullins, research technician at the Giga-to-Nanoelectronics Centre, for the maintenance of the laboratory necessary to the completion of my thesis.

Finally, I would like to thank my group members for their constructive criticism, and positive feedback during the writing period of my thesis. In particular, I would like to thank Qi Wang for his contribution and help through useful suggestions.

Table of Contents

List of Figures

List of Tables

Chapter 1: Introduction

Since the replacement of the vacuum tube based devices in the middle of the 20th century by solid state electronics, inorganic semiconductors such as Si and Ge have been the dominant materials for the manufacturing of electronic devices. However, the more recent development and understanding of a new class of semiconductors based on conjugated carbon chains have made organic electronics an emerging and attractive alternative technology.

The applications of organic electronics are various and some of them, such as Organic Light-Emitting Diodes (OLEDs) [1-4], Organic Thin Film Transistors (OTFTs) [5-9], and Organic Solar Cells (OSCs) [10-12] achieved encouraging performances. OLEDs, for instance, have entered the commercial market in devices such as displays and solid state lighting systems and possess very promising properties such as faster refresh rates, wider viewing angles, and better color contrast. *Figure 1.1* shows several applications of organic electronics [13-17].

Figure 1.1: Applications of organic electronics. From left to right, top to bottom: organic flexible solar panel [13]; Samsung OLED phone prototype [14]; Transparent and flexible green OLED [15]; LG OLED 55-inch OLED television [16]; Philips Lighting's GL350 OLED panels [17].

Similarly, organic semiconductors are very attractive for thin film Organic Photodetectors (OPDs) because they possess a number of desirable attributes for optical sensing including high absorption coefficients over visible and ultraviolet wavelengths and compatibility with large-area deposition processes such as ink-jet, screen printing, and solution processing.

1.1. **Organic Semiconductors**

The materials used in OPDs have a conjugated π-electron system formed by the p-orbitals and sp^2-hybridized carbon atoms in the molecules. Carbon in C=C bonds (e.g. Ethylene) is hybridized differently than in C-C bonds (e.g. Methane, Ethane) because the 2s orbital is mixed with only two of the three available 2p orbitals. This results in only three hybridized orbitals (sp^2 hybridization) with a trigonal orientation. In comparison, carbon in a C-C bond is sp^3-hybridized and 4 sp^3 orbitals are formed with a tetrahedral orientation. In an sp^2-hybridized carbon atom, one p orbital remains, which is perpendicular to the plane containing the hybridized orbitals. The energy diagram of the sp^2 hybridization in ethylene and the spatial distribution of an sp^2-hybridized carbon atom are displayed in *Figure 1.2* [18].

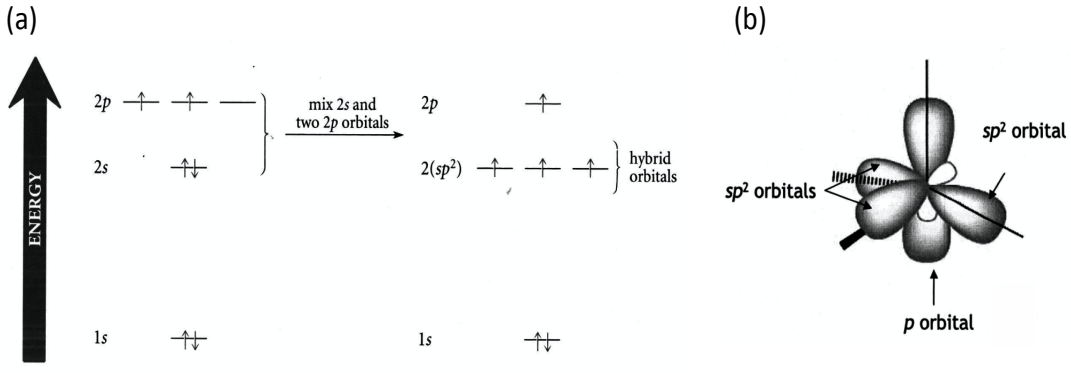

Figure 1.2: (a) Energy diagram of the sp^2 hybridization in ethylene and (b) the spatial distribution of an sp^2-hybridized carbon [18].

Organic molecules comprise of single and double bonds. Single bonds are σ covalent bonds formed by two sp^2 hybrid orbitals belonging to two adjacent carbon atoms. Double bonds consist of two covalent bonds, one σ-bond, identical to the single bond, and one π-bond which is formed by the overlap of two adjacent p orbitals. In conjugated systems, π-bonds overlap with adjacent π-bonds resulting in a stabilizing electron delocalization, responsible of the conduction in organic molecules. In the special case of benzene, as demonstrated in *Figure 1.3,* the delocalization of electrons over the carbon ring leads to a resonance effect making aromatic rings very attractive for organic semiconductors.

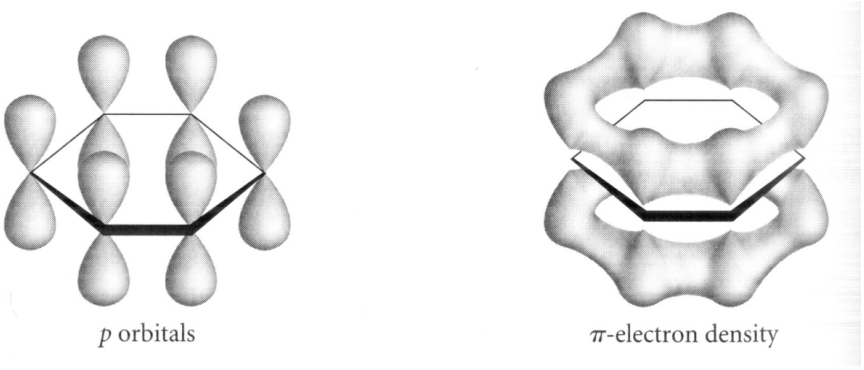

Figure 1.3: Resonance effect in benzene molecules.

Long conjugated molecules exhibit a significant electron delocalization that increases the orbital splitting and creates continuous energy bands as shown in *Figure 1.4* [19]. Therefore long conjugated molecules exhibit large energy bands and reduced band gaps compared to short ones.

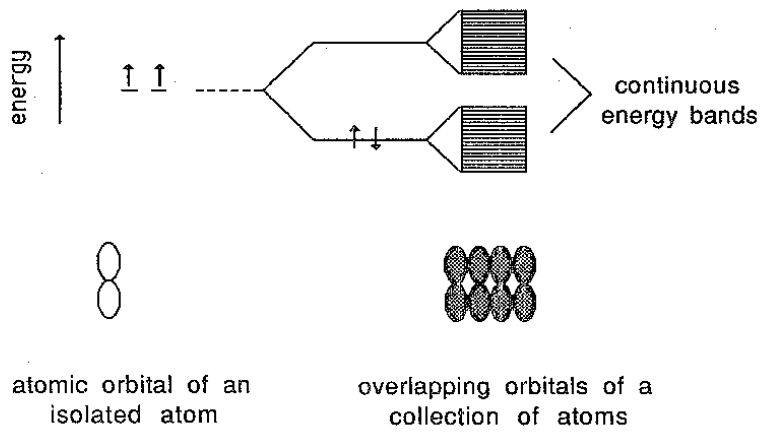

Figure 1.4: Orbital splitting and creation of continuous energy bands in organic semiconductors [19].

Compared with the σ-bonds being the backbone of the molecules, the π-bonds are significantly weaker. Consequently, the lowest electronic excitations of the conjugated molecules are the π-π* transitions with an energy gap typically between 1.5 and 3 eV. This results in a strong absorption in the ultraviolet and visible spectral range. The π-orbital in the π-π* transitions is called the Highest Occupied Molecular Orbital (HOMO), and the π*-orbital is the Lowest Unoccupied Molecular Orbital (LUMO). The energy difference between the HOMO and LUMO is generally considered as being the optical bang gap of the molecule. However, organic films are made of multiple molecules that are weakly bounded together via Van Der Waals interactions. π-π stacking between neighboring molecules, due to intermolecular overlapping of p-orbitals in π-conjugated systems, might occur and lead to more orbital splitting. Therefore, π-π stacking can widen the energy bands and reduce the optical band gap as shown in *Figure 1.5* [20].

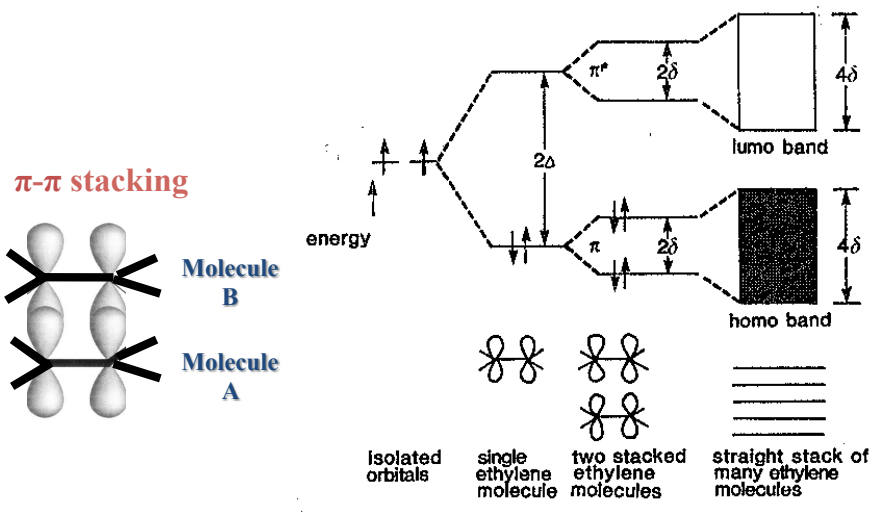

Figure 1.5: Widening of the continuous bands and reduction of the band gap because of π-π stacking in organic thin films [20].

Organic materials are attractive for optoelectronics devices since it is possible to tune both their electrical and optical properties. The transport of carriers in organic films and the role of π-π stacking are described in a following section.

Two types of materials are used in OPDs: small molecules (organometallic chelates, conjugated dendrimers, etc.) and polymers (poly(p-phenylene vinylene), polyfluorene, etc.) as displayed in *Figure 1.6.* Small molecules based OPDs are typically fabricated using thermal evaporation. A thermal evaporation process enables the growth of homogeneous organic thin films with a good control of the deposition parameters and permits to design as well complex multi-layer structures. Nevertheless, thermal evaporation is highly material consuming which increases the costs of fabrication. Some other techniques, such as organic vapor phase deposition, have been investigated to reduce material waste. On the other hand, polymers based OPDs are generally prepared by spin-coating or printing techniques. These solution-based processes are very attractive for the electronics industry to form large-area films at reduced costs. However, the control of the growth has still to be enhanced and the design of complex structures is

hardly achieved leading in general to lower efficiency devices in comparison to small molecules based OPDs.

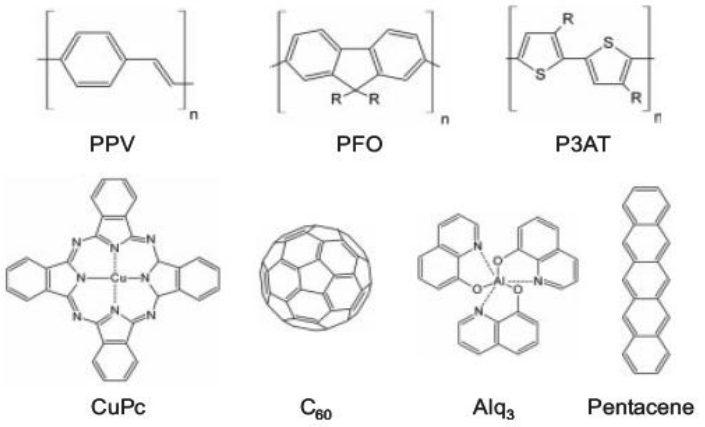

Figure 1.6: Some organic molecules and polymers widely used in OPDs [21].

1.2. Overview of OPDs

OPDs are part of the general family of the organic light harvesting devices. The strong optical response of organic materials across the visible spectrum initially led to their use in the development of organic photoreceptor drums for xerography processes, in which exposure to light leads to a discharge of a pre-charged organic photoconductor [22]. More recently, they have been used for the development of solar cells [23] and thin film OPDs [24].

An OPD is a device capable of converting light into an electrical signal. An OPD, in general, utilizes a vertical device architecture where a thin film, made of photoactive organic semiconductor layers, is sandwiched between top and bottom electrodes. One of these contacts is transparent at the wavelength of operation and is commonly made of indium tin oxide (ITO) sputtered on a glass substrate, as shown in *Figure 1.7.* Exposure to light leads to the formation of excited states in the active layers, widely called

excitons. The excitons dissociate then into free carriers (holes and electrons) that are able to travel through the layers and thus generate a current between the two electrodes in an external circuit under some applied voltage. In order to increase its performances, an OPD usually operates in the reverse bias regime, i.e. the anode (usually made of ITO with a high work function) and the cathode (commonly made of a low work function metal such as silver or aluminum) being negatively and positively biased, respectively. To investigate the photoresponse of an OPD, both the currents under dark and illuminated conditions (denoted in the rest of the thesis by I_d and I_{ph}, respectively) are measured over a voltage range (I-V characteristics).

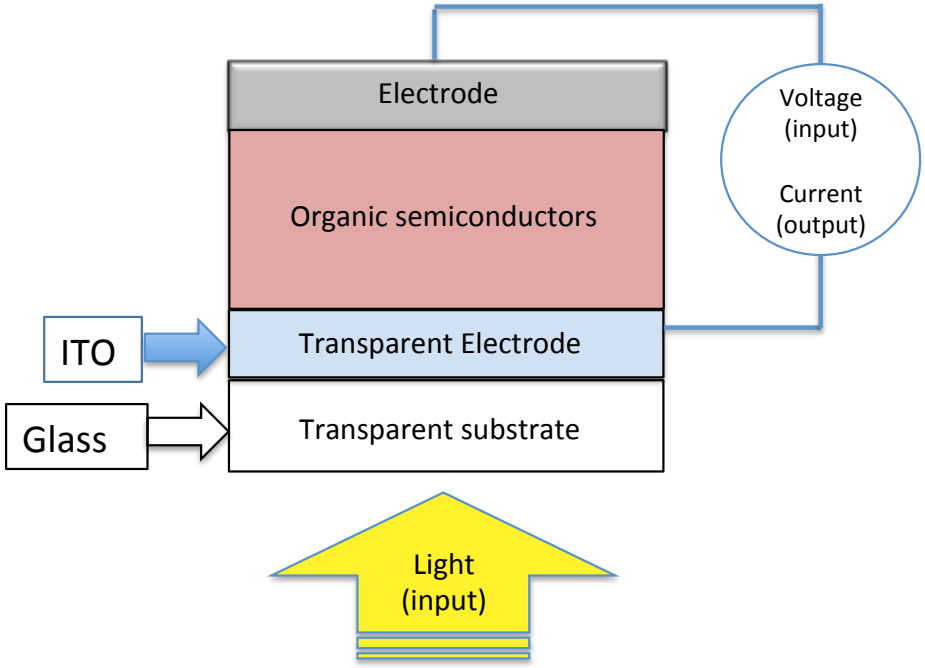

Figure 1.7: Typical structure of an OPD.

Several figures of merit, listed in *Table 1.1*, are used to characterize the performances of an OPD:

Sensitivity	Ratio of the photocurrent level to the dark current level at a given voltage.	$\frac{I_{ph}}{I_d}$
External Quantum Efficiency (EQE)	Ratio of the number of charge carriers collected l to the number of incident photons at a given wavelength.	EQE=$\frac{I_{ph}/q}{P_0/h\nu}$
Specific Detectivity (D^*)	Signal-to-noise ratio assuming the shot noise from the dark current is the major contribution to the noise	$D^* = \frac{R}{\sqrt{2.q.J_D}}$
Rise (τ_R) and decay (τ_D) times	τ_D (τ_R) is the time in which the photocurrent drops from 90% to 10% (increases from 10% to 90%) of its maximum value, when the device is excited with rectangular light pulses.	Determined experimentally.
Bandwidth (f_{3dB})	Frequency at which the photocurrent is 3dB lower than the low-frequency response. Calculated by taking the inverse of the time required for a pulse of photocurrent to decay to 1/e of its initial value.	Determined experimentally.

Table 1.1: Figures of merit of an OPD.

where I_{ph} is the photocurrent level (A)
I_d is the dark current level (A)
q is the absolute value of electron charge (C),
P_0 is the power of the incident light (W),
R is the photocurrent responsivity (A/W),
J_D is the dark current density (A/cm^2)

1.3. Operation mechanism of an OPD

The operation mechanism of an OPD includes three basic step: photon absorption and creation of Frenkel exactions; exciton dissociation into free charge carriers; and charge carriers collection. The external quantum efficiency (EQE) of an OPD can be estimated as being $EQE = \eta_{absorption} \cdot \eta_{exciton\ dissociation} \cdot \eta_{collection}$ and is directly proportional to the efficiencies of each of these steps. Understanding the device physics is crucial for improving its performances and therefore these three mechanisms will be introduced in detail in the following sections.

1.3.1. *Light Absorption and Exciton Creation*

1.3.1.1. Beer-Lambert Law

When an electromagnetic radiation hits an organic sample, photons are absorbed by organic molecules, creating thus excited states, widely named excitons. Absorption is a crucial stage of OPDs' operation because it affects not only their efficiencies, but also their sensitivity and selectivity (high response at a particular wavelength). The appropriate choice of organic materials as well as their configuration in the device structure highly influence the application (infrared, visible, or ultraviolet detection) and $\eta_{absorption}$ (ratio of the number of created excitons to the number of absorbed photons) of OPDs.

The bulk absorption characteristics of a compound can be represented by the Beer-Lambert empirical law $I = I_0.10^{-\alpha l}$ where I_0 is the intensity of the incident monochromatic radiation, I is the intensity of transmitted radiation, α is the absorption coefficient of the compound at a particular wavelength, and l is the length-path of the radiation through the sample, as drawn in *Figure 1.8* [25].

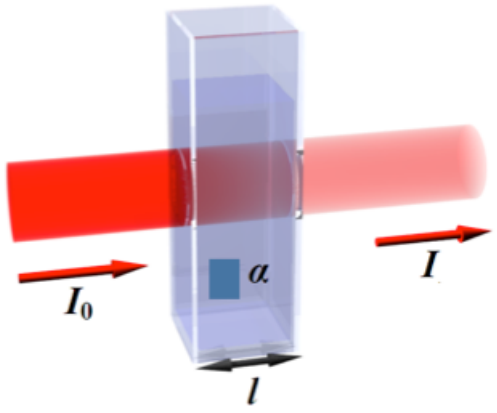

Figure 1.8: Illustration of the Beer-Lambert law [24].

1.3.1.2. Oscillator Strength, Transition Moment and Selection Rule

However, the absorption of a photon by organic molecules being fundamentally visualized as an electronic transition, i.e. as an excitation of an electron from a molecular orbital to another one with higher energy, it is useful to characterize the absorption of a sample using a more theoretical quantity, the oscillator strength *f*, which is given by the integral [26]:

$f = 4.315.10^{-9} \int \varepsilon . d\nu$ where ε is the extinction coefficient and υ is the frequency.

The oscillator strength, which gives the integrated intensity of absorption over a whole energy band, is found to be proportional to the square of the transition moment (T.M.) defined as $T.M. = \int \Psi_i . \boldsymbol{\mu} . \Psi_f d\tau$, where Ψ_i and Ψ_f are the total wavefunctions (nuclear and electronic) of the initial and final states, respectively; and $\boldsymbol{\mu}$ is the dipole moment operator [26]. Consequently, the absorption of a photon by an organic molecule is directly related to the magnitude of the T.M. which determines whether a transition is allowed $(T.M. \neq 0)$ or forbidden $(T.M. = 0)$, which is the basis of the so-called "selection rule".

Because the wavefunctions of molecules are difficult to evaluate, the *Born-Oppenheimer Approximation* has been introduced to simplify the expression of the transition moment and enables to factorize the total wavefunction of the molecule into a nuclear (vibrational) wavefunction θ and an electronic wavefunction ψ $(\Psi = \theta . \psi)$, the latter being a linear combination of electronic orbitals ϕ. Finally, the electronic orbitals ϕ can be factorized into a product of space (φ) and spin orbitals (S). The transition moment

can hence be factorized into three terms and this approximation allows identifying, thanks to symmetry analyses, whether an electronic transition is allowed or forbidden:

$$T.M. = \int \theta_i \, \theta_f d\tau_N \, . \int S_i \, S_f d\tau_S \, . \int \varphi_i \, . \boldsymbol{\mu} . \varphi_f d\tau_e$$

where subscripts *N*, S, *and e* refer to nuclei, spin, and electrons [26].

- *Vibrational Overlap Integral (Franck-Condon principle)* $\int \theta_i \, \theta_f d\tau_N$*:*

Molecules being considered as simple harmonic oscillators, it is possible to estimate the nuclear wavefunctions associated with each vibrational level (oscillating curves plotted as a function of the internuclear separation in *Figure 1.9 (a*) [26]) by solving the appropriate Schrodinger equation. The vibrational overlap integral will be maximum, and therefore T.M. will be maximum, when the overlap between the vibrational wavefunction of the ground state (at an energy $v'' = 0$) and one vibrational wavefunction of the excited state (energy v') is significant, making this particular transition the most probable for absorption. *Figure 1.9 (b)* [26] shows the particular example of a molecule exhibiting a higher absorption coefficient for the transition 0→2 due to a better vibrational overlap. In other terms, the vibrational overlap integral represents the change in geometry (shift of the equilibrium internuclear separation) of the molecule after excitation due to the stretching of a bond by promoting an electron usually from a bonding to an anti-bonding orbital.

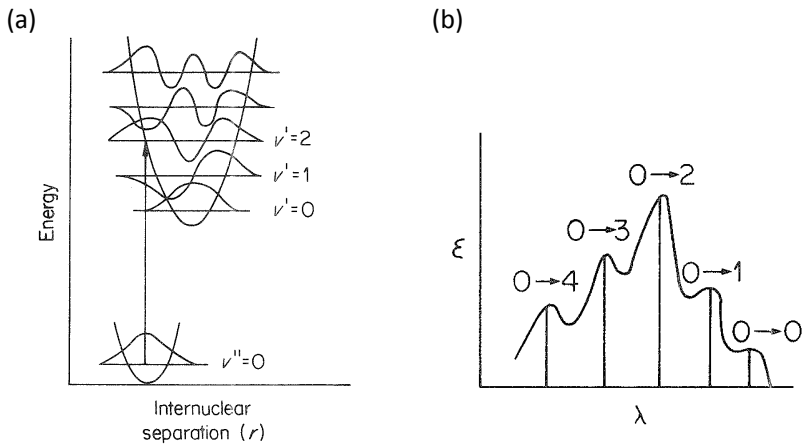

Figure 1.9: (a) Vibrational levels for the ground ($\boldsymbol{v''}$) and excited ($\boldsymbol{v'}$) states, the arrow representing the strongest absorption transition and (b) absorption coefficient spectrum of an organic molecule [26].

This quantum mechanical discussion is the basis of the *Franck-Condon Principle,* depicted in *Figure 1.10* [26]*,* which states that, the electronic transitions being fast, no change in nuclear position or nuclear kinetic energy occurs during the transition. The transition can be represented by a vertical line connecting the two potential energy surfaces, and the most probable transition will be to that vibrational level with the same internuclear distance at the turning point of the oscillation (line AY in the case of absorption). A transition represented by a line AX would be very improbable because the molecule, in arriving at point X, would have suddenly acquired an excess of energy given by XY. The line ZB represents the most probable transition in the case of emission, which will not be discussed in this work.

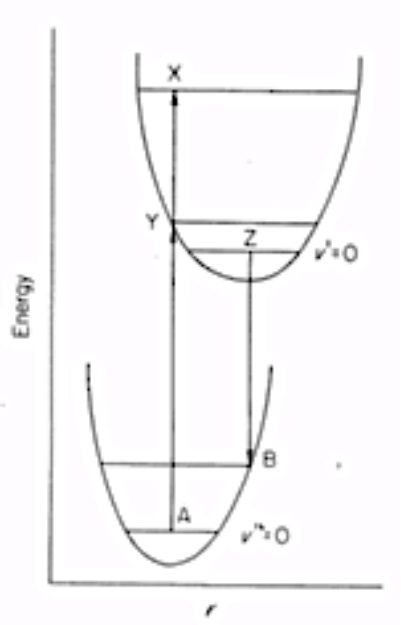

Figure 1.10: Illustration of the Franck-Condon Principle [26].

- *Spin factor* $\int S_i S_f d\tau_S$*:*

There are three possible spin transitions that are either allowed or forbidden depending whether the spin multiplicity of the molecule is conserved or changed:

Singlet ⟶ Singlet transitions:	Allowed
Triplet ⟶ Triplet transitions:	Allowed
Singlet ⟶ Triplet transitions:	Forbidden

Singlet ⟶ Triplet transitions can nevertheless occur thanks to spin-orbit coupling due to the presence of heavy atoms in the molecules, mechanism which is widely seen and used in phosphorescent OLEDs, but these transitions are not governed by the selection rule.

- *Electronic transition moment (E.T.M.)* $\int \varphi_i \,.\, \boldsymbol{\mu}.\, \varphi_f d\tau_e$*:*

The E.T.M. depends on both (i) the symmetries of the atomic orbitals involved in the transition and (ii) the molecular orbitals spatial overlap:

(i) Symmetries of atomic orbitals:

$\boldsymbol{\mu}$ being a vector operator, the E.T.M. can be resolved along the three Cartesian space directions: E.T.M. = $E.T.M._x + E.T.M._y + E.T.M._z$. A transition will be forbidden if the three spatial component integrals are zero. For example, the transition 1s ⟶ 2p, described in *Figure 1.11* [26], is allowed since $E.T.M._x$ is not zero (integral of a product of two odd functions and one even function).

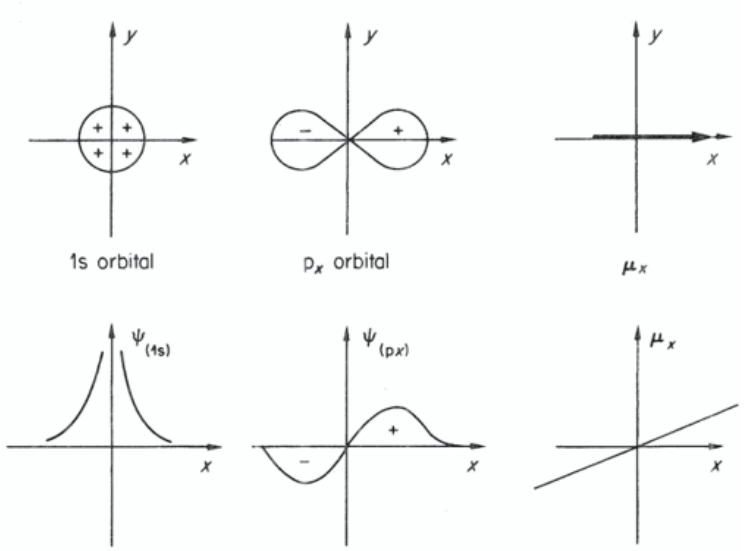

Figure 1.11: Symmetries of 1s and 2p orbitals and spatial representation of the vector operator [26].

(ii) Molecular orbitals spatial overlap:

A transition can be forbidden even though it is symmetry-allowed if the two molecular orbitals are spatially distant from each other as can be seen in *Figure 1.12* [26] in the case of the pyridine molecule, for the n ⟶ π^* transition. However, in aromatic compounds, which are widely used in organic optoelectronic devices, the $\pi \longrightarrow \pi^*$

transitions between the HOMO and LUMO levels are usually allowed on spatial overlap grounds.

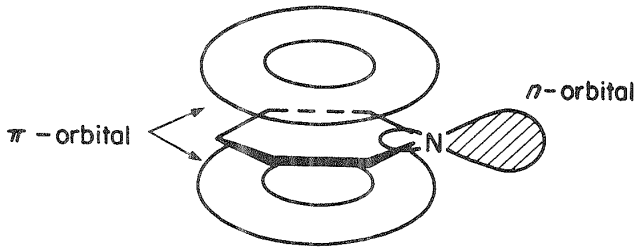

Figure 1.12: Molecular orbitals spatial overlap of pyridine [26].

1.3.2. *Exciton Nature and Dissociation*

1.3.2.1. Exciton Nature

Absorption of a photon by an organic molecule creates an exciton that is defined as a bound state of an electron, in a non-ground energy level, and hole. The electron and the hole are attracted to each other by the electrostatic Coulomb force [27] and are capable of diffusing and migrating together. Depending on the distance and the interaction between the electrons and holes, excitons can be classified as: (a) Frenkel excitons, (b) Wannier-Mott excitons and (c) Charge-transfer excitons (*Figure 1.13*) [28].

Frenkel exciton (*Figure 1.13 (a)*), typical of organic small molecules-based semiconductors, corresponds to an electron-hole pair localized usually on a single molecule. The interaction between the electron and the hole may be strong which leads to a high binding energy on the order of 0.1 to 1eV. Frenkel excitons tend thus to have radii comparable to the size of a single molecule (typically < 5 Å), or smaller than the intermolecular distance. Because the hole and the corresponding electron are located on

the same molecular site due the high intermolecular distances, Frenkel excitons are neutral and the electron and the hole are moving as a whole.

Wannier excitons (*Figure 1.13 (b)*), on the other hand, are found typically in crystalline materials with strong molecular interactions and high dielectric constants. Because of a significant potential overlap between neighboring lattice points in such materials, Coulumbic interactions between the electron and the hole are reduced. They hence show large radii of $\sim 40 - 100\text{Å}$ (whose length is many times the length of the lattice constant) and relatively low binding energies ($\sim 10meV$) which makes their dissociation into free electrons and holes facilitated.

Intermediate or charge-transfer excitons (*Figure 1.13 (c)*), with intermediate radii, can also be generated in organic materials, to a smaller extent with respect to Frenkel excitons. They represent an electronically excited, neutral, polar crystal state where the exciton radius is only one or two times the lattice constant (the promoted electron is transferred to nearest or next-nearest neighboring molecular sites but still remains correlated to its parent hole).

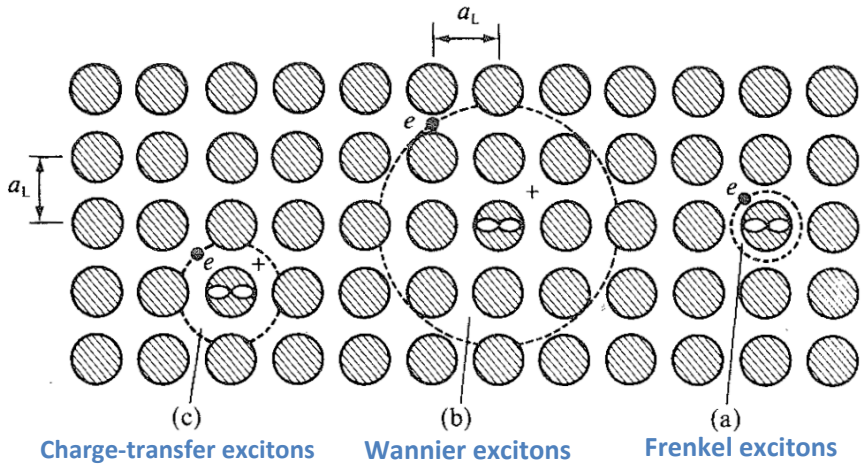

Figure 1.13: (a) The small-radius Frenkel exciton in which the radius is small in comparison with a lattice constant (b) The large-radius Wannier-Mott exciton with a large radius (c) The intermediate or charge-transfer exciton.

1.3.2.2. Exciton Dissociation

The exciton dissociation rate is critical in OPDs efficiency and $\eta_{e-h\ dissociation}$ is defined as the ratio of the number of free carriers created to the number of excitons formed. Frenkel excitons have a finite probability of dissociation that could be either intrinsic or sensitized. Both types of dissociation involve the formation, before the dissociation into free carriers, of a Geminate electron-hole pair (e-h pair), bound state of an electron and hole weaker than an exciton.

Two types of intrinsic dissociation are observable: (a) the Internal Conversion Mechanism and (b) the Onsager Mechanism, both of them being highly electric field-dependent and described in *Figure 1.14*. In the case of process (a), the exciton first relaxes to the excited state with the lowest energy by internal conversion. The formation of a Geminate e-h pair, highly field-induced, might then occur before its dissociation into free carriers. In the case of process (b) however, the Geminate e-h pair is formed via an auto-ionization process of the hot exciton precursor (no relaxation to the lowest excited state). This process depends therefore on the wavelength of absorption and the field-dependence of this process arises from the dissociation, and not the formation, of the Geminate e-h pair.

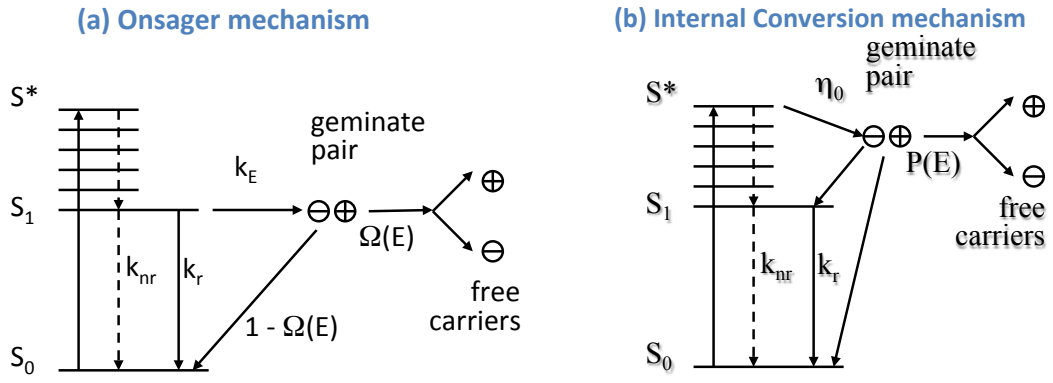

Figure 1.14: (a) Onsager and (b) Internal Conversion dissociation mechanisms.

In the case of sensitized dissociation, the free carriers are generated due to the charge transfer of a host molecule excitons to a guest sensitizer. This type of dissociation can either be bulk sensitized or surface sensitized, widely used in organic light harvesting devices. During the charge transfer process, the molecule acquiring the hole from the exciton dissociation is called the donor (D) molecule and the molecule acquiring the electron is called the acceptor (A) molecule. The efficiency of this type of dissociation involving two species depends first on the ability of the exciton to diffuse to a D/A interface and second on the efficiency of the charge transfer at the interface.

An exciton can migrate randomly [29] in the semiconductor and is thus characterized by its diffusion length L_D (average distance an exciton can move from the point of generation until it recombines), which is related to the mobility μ of the organic semiconductor and the exciton lifetime τ by the equation $L_D = \sqrt{\mu.\tau}$. L_D is a property of a single organic semiconductor and is generally very short, from 5 to 30nm for the most common organic semiconductors [11] leading to a high recombination rate in OPDs if the exciton does not encounter a dissociative site in the range of its diffusion length.

The dissociation efficiency of an OPD using a D/A heterojunction (HJ) is also dependent on the charge transfer efficiency at the organic-organic interface. In contrast to inorganic HJs, organic HJs generally do not have a significant amount of free charges that redistribute when materials are brought into contact [30]. Furthermore, their energetics are rarely influenced by the crystalline morphology at the interface since most of these van der Waals bonded materials do not require lattice matching to form ordered structures [31]. An energy level diagram of an organic heterojunction between a D and an A is proposed in *Figure 1.15* [32]. The difference between the ionization potential (IP) and electron affinity (EA) is known as the transport gap, (E_{tran}). The optical energy gap of each material, E_{opt}, is defined as the position of the low-energy absorption edge. The exciton binding energy (E_B) of each material is equal to the difference between E_{tran} and E_{opt} The interfacial interface is facilitated when the offset between the HOMO of the D molecule and the LUMO of the A molecule is greater than E_B.

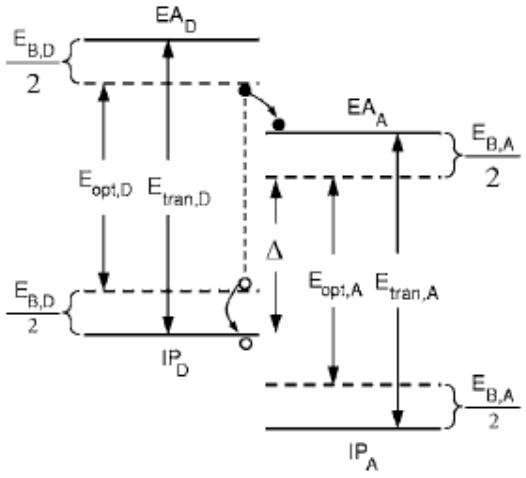

Figure 1.15: Proposed energy level diagram of an organic heterojunction between a donor (D) and an acceptor (A) layer. IP and EA are the ionization potential and electron affinity, respectively. The process of charge transfer of an exciton from D→A is also illustrated. [32]

If the dissociation efficiency is low, the exciton may undergo deactivation processes, i.e. radiative or non-radiative decays of the exciton to the ground state before dissociation intro free carriers. These transitions are summarized in a Jablonski diagram (*Figure 1.16*) [33] in which S_0 is the ground state, S_1 is the first singlet excited state, S_2 is the second singlet excited state, T_1 is the first triplet excited state, VR is vibrational relaxation, ISC is intersystem crossing, and IC is internal conversion, respectively.

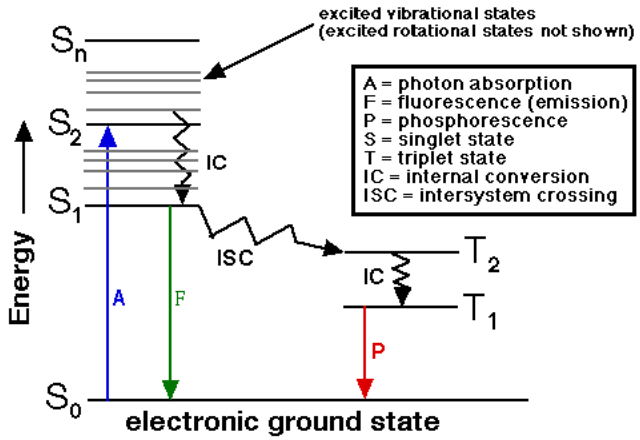

Figure 1.16: Jablonsky diagram [33].

In radiative transitions, represented by solid lines in a Jablonski-diagram, an excited species goes from a higher excited state to a lower one with the emission of a photon. There are three distinguishable processes in this radiative category:

(1) Fluorescence results from a rapid radiative transition (~ns) between states of the same spin multiplicity, typically $S_1 \rightarrow S_0$.

(2) Phosphorescence is the result of a transition between states of different multiplicity, typically $T_1 \rightarrow S_0$. The rate constant of phosphorescence is usually much smaller than that of fluorescence due to the fact that phosphorescence is spin forbidden. However, the rate constant of phosphorescence can be dramatically increased by adding

heavy atoms into the materials, which enables fast triplet dissipation due to strong spin-orbital coupling. Such molecular engineering is widely used in phosphorescent OLEDs.

(3) Delayed fluorescence (not represented in the figure), which is not shown in the Jablonski-diagram, differs from fluorescence because the measured rate of decay of emission is less than that expected from the $S_1 \rightarrow S_0$ transition. It results from either a process named triplet-triplet annihilation or the recombination of trapped charges.

On the other hand, non-radiative transitions, represented by dotted lines in a Jablonski-diagram, occur between isoenergetic (degenerate) vibrational-rotational levels of different electronic states. Since there is no change in the total energy, no photon is emitted. There are two processes in this non-radiative category:

(1) Internal conversion is a non-radiative transition between isoenergetic states of the same multiplicity.

(2) Intersystem crossing is a non-radiative transition between states of different multiplicity.

1.3.3. *Charge Carrier Collection*

The charge carrier collection efficiency is mainly dependent on the charge carrier transport in OPDs. Once the excitons are dissociated, the free electrons and holes are transported across the organic layers. In contrast to inorganic semiconductors in which the carriers experience an intramolecular band model-like transport due to the strong covalent bonding, amorphous organic solids exhibit in general an intermolecular hopping model-like transport. Organic semiconductor molecules are bonded together by relatively weak Van der Waals forces and the charge carriers are localized in individual molecular

sites. The conjugated π-electron system formed by the p-orbitals of sp^2-hybridized carbon atoms in organic molecules enables π –π stacking of molecules that helps the conduction of carriers. However, the intermolecular distances remaining large ($> 10Å$), and the intermolecular interactions being thus weak due to an insignificant overlap between molecular wavefunctions, the energy bands in an organic semiconductor are narrow and the band gap is wide. Therefore the transport of free carriers occurs via hopping between localized states reducing the mobility ($\mu\,(organic) < 10^{-2}$ cm^2/V.s), and thus the conductivity, of organic materials in comparison to their crystalline counterparts ($\mu\,(crystalline) > 1$ cm^2/V.s).

For organic amorphous solids, one should consider locally varying polarization energies due to different molecular environments which lead to a Gaussian density of states (DOS) N(E) for the distribution of transport sites as shown in *Figure 1.17* [34].

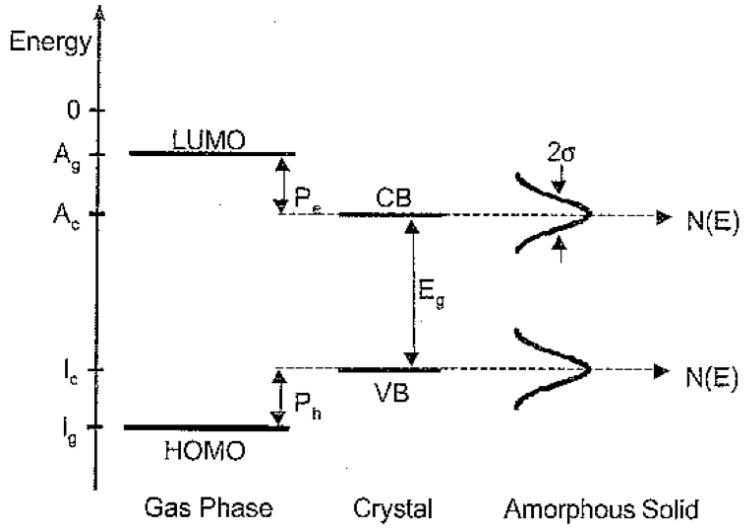

Figure 1.17; Gaussian distribution of density of states in organic semiconductors [34].

The organic materials conductivity is often described using the Poole-Frenkel (PF) model which illustrates the electric field (F) dependence of an organic semiconductor's mobility:

$$\mu(F) = \mu_0 . \exp(\beta_{PF} . \sqrt{F}) \text{ with } \beta_{PF} = \sqrt{\frac{q^3}{\pi\varepsilon}}$$

where μ_0 is the zero-field mobility; β_{PF} is the PF slope; q is the unit of electronic charge, and ε the dielectric constant. One can notice that the PF mobility depends on the zero-field mobility which is constant at a given temperature and only depends on the intermolecular potential barrier and thus on the intermolecular separation. One would expect a flat molecule with significant π–π stacking to have a higher mobility than an angular molecule. The term β_{PF} is closely related to the organic film spatial disorder, which is as well directly dependent on the molecular packing [35]. For example, AlQ_3[1] films mobility is significantly increased when the electrical field is increased (β_{PF} in the case of AlQ_3 is high). In contrast, the BPhen[2] film exhibits a significantly higher and almost constant mobility while increasing the electric field, i.e β_{PF} in the case of BPhen molecules is very small. The difference is due to the fact that BPhen molecules are flat molecules enhancing the π–π stacking, and therefore the order in Bphen films, as summarized in *Figure 1.18*. A more accurate model would also take into account an energetic disorder arising from the Gaussian distribution of energetic states in amorphous organic films.

[1] AlQ_3 : Tris(8-hydroxyquinoline) aluminum
[2] BPhen: Bathophenantroline

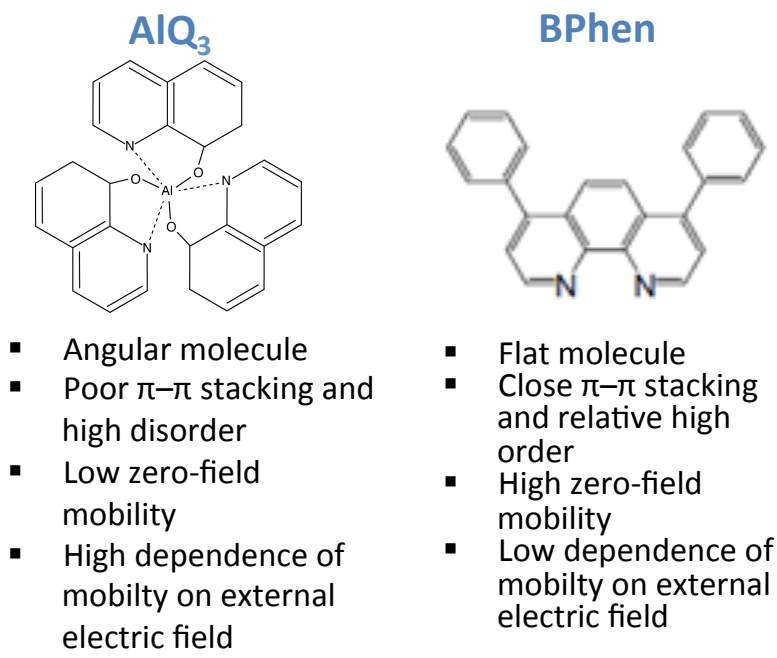

Figure 1.18: Comparison between AlQ_3 and BPhen mobility evolution with external electric field.

The carriers are transported across the organic layers to the metallic contacts where they get extracted. OPDs charge carriers collection is electric-field assisted. However, the photo-sensitivity of an OPD is proportional to the ratio I_{ph}/I_d at a given wavelength, and therefore is optimized for low I_d values. The injection of free carriers when applying a voltage needs to be minimized in order to only obtain the current due to the photoresponse of the organic layers. Hence, vertical OPDs are usually reverse biased and use rectifying contacts in order to limit the injection and the dark leakage current.

1.4. **Advances in OPDs**

The use of organic materials for photodetectors was motivated by a number of advantageous properties. OPDs can be fabricated on a variety of substrates, including low-cost, flexible foils and may provide photodetection over large areas. Moreover, with the advances of OLEDs, OTFTs and OSCs, there is a need now for efficient, high

bandwidth OPDs that might enable in the future to build molecular organic photonic integrated circuits. Consequently, a lot of efforts have been made in order to improve the performances of OPDs.

The development of OPDs was stimulated by the discovery in 1992 by *Sariciftci et al*. [36] of efficient photo-induced charge transfer between polymers and small organic molecules, more precisely between conducting polymers and buckminsterfullerene C_{60} (and its derivatives), which separates very efficiently and very quickly (in the range of the subpicosecond) electrons and holes before early recombination. The first efficient OPDs were then made of bilayer structures comprising a conducting polymer-C_{60} heterojunction [37, 38].

Photovoltaic effects have been also shown in OPDs made of a single polymer layer with, however, lower efficiencies. For example, *Yu et al.* (1994) [39] first characterized the photoresponse of diodes comprising a single polymer active layer and reported its dual function as both an emitting and sensing device. A diode with a structure ITO/MEH-PPV[3]/Ca showed a photoresponse increasing significantly under reverse bias. At -10 V bias, the detectevity was 0.045 (A/W) under illumination of 1 μW/cm^2.

Nevertheless, seeing that the D-A interface facilitates greatly the exciton dissociation in OPDs via charge transfer, the next improvements were achieved by sensitizing in the bulk a conductive polymer donor with C_{60} (and its derivatives) used as acceptor material [38, 39, 40, 41]. This enabled to increase the interfacial area and to design new kinds of OPDs based on bulk heterojunctions (BHJs). Even though the dissociation efficiency was significantly improved in BHJ OPDs improving their overall

[3] MEH-PPV: poly[2-methoxy-5-(2'-ethylhexyloxy)-p-phenylene vinylene]

efficiency, the collection efficiency was however decreased due to the poor transport of free carriers that undergo severe charge trapping in BHJ systems.

In order to reduce the charge trapping in BHJ OPDs, it was necessary to enhance the control of the morphology of the BHJ active layer [42]. Through the control of the phase separation into an interpenetrating bicontinuous of D and A phases, both hole and electron transports can be enhanced. A tradeoff however has to be found. On one hand, the extension of the D/A interface has to be maximized in order to allow excitons to diffuse to the interface and to dissociate. On the other hand, the two phases have to form a continuous interpenetrating network to allow the percolation of charges toward their respective electrodes. A certain number of ways to control the blend morphology have been developed. These include both deposition and post-deposition procedures, such as an appropriate choice of solvent for the spin-coating [43], slow drying of spin-coated films [44], thermal annealing [45], and vapor annealing of blends [46].

Small molecule OPDs have the advantages of allowing multilayer structures with no need of considering mutual solubility issues in multilayer polymeric devices. Therefore, more complex device structures become possible in comparison to polymers based OPDs. For example, *Peumans et al*. (2000) [47] reported a high efficiency and high bandwidth OPD incorporating an ultrathin D-A alternating multilayer stack as schematized in *Figure 1.19* (the BCP[4] layer acting as a hole blocking layer preventing exciton quenching at the contacts).

[4] BCP : bathocuproine

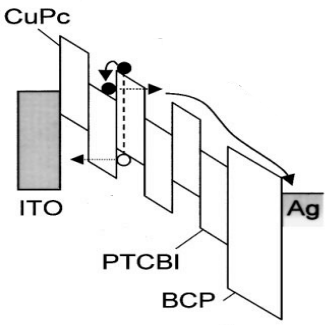

Figure 1.19: Schematic energy-level diagram of an alternating donor–acceptor multilayer photodetector device under reverse bias. The process of exciton dissociation, followed by carrier separation by tunneling is illustrated [47].

The OPD exhibited a high EQE ~75% at a reverse bias of -10V for a structure comprising 64 layers being alternatively CuPc[5] donor layers and PTCBI[6] acceptor layers of only 5Å each (the total thickness of the active layers being 32nm). This high efficiency was attributed to an improvement in both exciton dissociation and carrier collection with decreasing the layers thicknesses; the former due to an efficient exciton diffusion to the D-A interfaces over distances in the order of a diffusion length (L_D being ~3Å for PTCBI) reducing the recombination rate; the latter due to an enhanced carrier tunneling through the energy barriers between layers (formed by the CuPc LUMO for electrons and the PTCBI HOMO for holes). Multilayer devices incorporating thinner layers have as well a faster response time and a higher bandwidth due to a shorter average exciton lifetime in the presence of many D–A interfaces. The response time is no longer limited by the exciton lifetime ($\sim 1ns$) but now by the faster charge carrier transport time.

Spectral response tunability has been achieved by developing as well complex small molecules based OPDs made of D-A bilayers (CuPc as D material and C_{60} as A

[5] CuPc: copper phthalocyanine
[6] PTCBI : perylene tetracarboxylic bisbenzimidazole

material) with opposed lateral thickness gradients along the longitudinal direction as reported by *J. Cabanillas–Gonzalez et al.* (2011) [48] and as shown in *Figure 1.20.* Gradual variation in layer thickness was achieved by using a mechanically controlled shutter with gradual displacement along the longitudinal direction. A gradual enhancement of the spectral response in the near-IR was observed by moving the illumination spot from the C_{60}-rich region towards the CuPc-rich region in 1 mm steps.

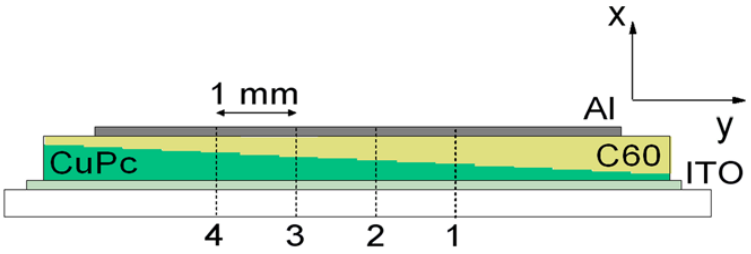

Figure 1.20: (a) Device configuration showing a thickness gradient of CuPc/C_{60} layers along the longitudinal direction (y-axis). Positions (1)–(4) are separated by 1 mm going from a C_{60}-rich to a CuPc-rich area [48].

In conclusion, milestone studies that led to the development of both polymer and small molecule based OPDs with performances comparable to inorganic PDs are presented here. It should first be mentioned that inorganic photodetectors made of GaN, Si, and InGaAs are being used for three important sub-bands, 250 to 400 nm (UV), 450 to 800 nm (visible), and 900 to 1700 nm (NIR) and require usually cooling to attain detectivities in the order of 10^{12} Jones which is power consuming. OPDs are now very attractive in terms of low-cost devices with wide spectral response ranges and offering promising performances, comparable and even better than inorganic ones as regards the detectivity. Indeed, the recent works of *Gong et al*. (2009) [49] and S-*H. Wu et al.* (2011) [50] made important breakthroughs for respectively polymeric and small molecule based OPDs as regards the spectral response range. The former useed an active layer made of a

small-band-gap π-conjugated polymer (PDDTT[7]) blended with a fullerene derivative ($PC_{60}BM$[8]), to obtain a very wide spectral response from 300 (UV) to 1450 nm (NIR). Besides, the OPD presented a multilayer structure, entirely fabricated by solution processes, and incorporated electron and hole blocking layers that enables to obtain a detectivity of greater than 10^{13} Jones at wavelengths from 300nm to 1150nm and greater than 10^{12} Jones from 1150nm to 1450nm. The latter demonstrated an OPD with a broad spectral response from 200 to 900nm by taking the advantage of more sophisticated device design in using small molecular materials. Indeed, photoresponse over the deep-ultraviolet and visible-near infrared regions could be independently optimized by jointing two donor/acceptor hetero-junctions which led to an EQE of ~20% over the entire spectral range and a detectivity of $\sim 10^{12}$ Jones.

1.5. **Lateral OPDs**

OPDs, in general, utilize a vertical device architecture where the photoactive organic semiconductor layers are sandwiched between top and bottom electrodes that provide electrical contact. More recently, an interest in utilizing a lateral device architecture instead of the vertical one, has emerged. In this architecture, the two contacts are positioned on the two sides of the photoactive material with respect to the direction of the incoming signal, separated by a small gap. In lateral OPDs, applying an electrical bias from an external source across the electrodes creates an electrical "channel" across the gap and thus allows the collection of photo-generated carriers

[7] PDDTT : polybis(thienyl)thienodia-thiazolethiophene
[8] $PC_{60}BM$: [6,6]-phenyl-C60-butyric acid methyl ester

produced by the exposure of the semiconductor material to illumination. As the charge carrier mobility of organic semiconductors is generally low ($<10^{-2}$ $cm^2/V.s$ for most organic semiconductors), the gap width must be kept small, typically a few tens of microns at most, in order to allow for sufficient charge collection. Lateral OPDs can be either bottom-contact (in which the two contacts are deposited on the substrate prior the deposition of the organic layers) or top-contact (in which the contacts are deposited after the deposition of the organics on the substrate and lie on top of them). Similarly, the illumination can come from both vertical directions: either from the side of the substrate (bottom illumination in the case of a top-contact lateral OPDs) or from the opposite side of the substrate and therefore through the gap (top illumination in the case of a top-contact lateral OPDs). The different types of architectures and illuminations are schematized in *Figure 1.21*.

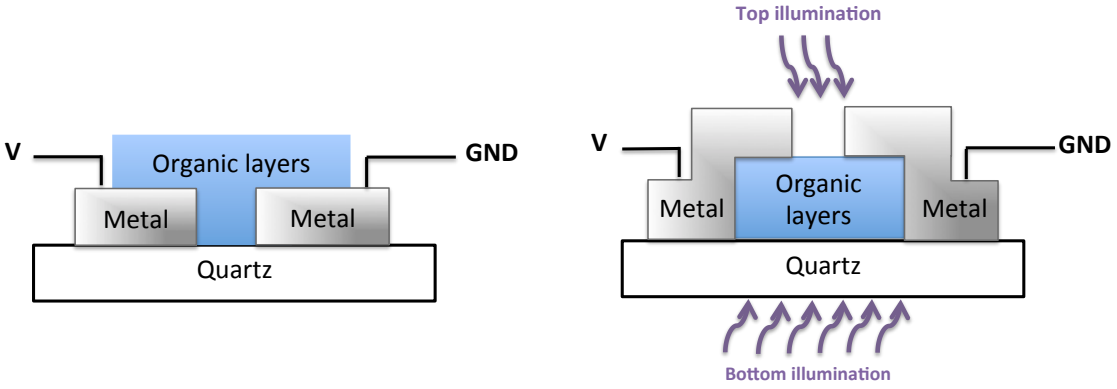

Figure 1.21: Schematics of bottom and top-contact lateral OPDs. The top and bottom illuminations are also represented.

As in the lateral OPDs the electrodes are not in the "optical path" of the signal, they (i.e. the electrodes) are not required to be transparent. This makes the lateral architecture particularly advantageous for UV or IR OPDs, since commonly used electrode materials, such as ITO or thin metal layers, often lack sufficient transmission at

these wavelengths. Therefore the rectifying contact metals can be freely chosen in order to lower dark currents since there is no need for a transparent electrode. Besides, the compatibility of planar photodetectors with the OTFT technology might be a premium feature for the development of low cost integrated organic optoelectronic devices.

A number of lateral OPDs with good performance were reported recently [50-55]. A planar OPD was first reported by *Natali et al.* (2002) [51] using a bottom-contact architecture under top illumination on which was deposited a single layer made of a material belonging to the class of neutral metal-dithiolenes. The central atom of the molecule can be varied between Ni, Pd, and Pt, which enabled to tailor the spectral absorption edge (for example, red-shift of 20nm in the peak of absorption by substituting Pt for Ni). *C. Ho et al.* (2008) [52] and *Caironi et al.* (2007) [53] investigated as well bottom-contact lateral OPDs using small molecule based HJ and post-treated polymeric BHJ, respectively. These lateral OPDs showed however lower performances compared to vertical ones and some efforts were made to improve them by exploring in particular hybrid lateral OPDs.

Indeed*, T. P. Osedach et al*. (2009) [54] investigated bottom-illuminated hybrid bottom-contact lateral OPDs, using a HJ made of a quantum dots (QD) donor layer on top of an organic semiconductor acceptor layer in contact with gold electrodes, as seen in *Figure 1.22*. The purpose was to separate light absorption occurring in the QDs layer from the charge transport taking place in the bottom organic layer. By choosing an appropriate wavelength of illumination and/or by tuning the optical response of the QDs layer (by selecting the type and the physical size of the nanocrystals), it is indeed possible to improve the performances of lateral hybrid OPDs by taking advantage of the efficient

absorption in the QDs layer and the better charge transport in the organic layer (QDs are strong electron traps and show poor conductivity).

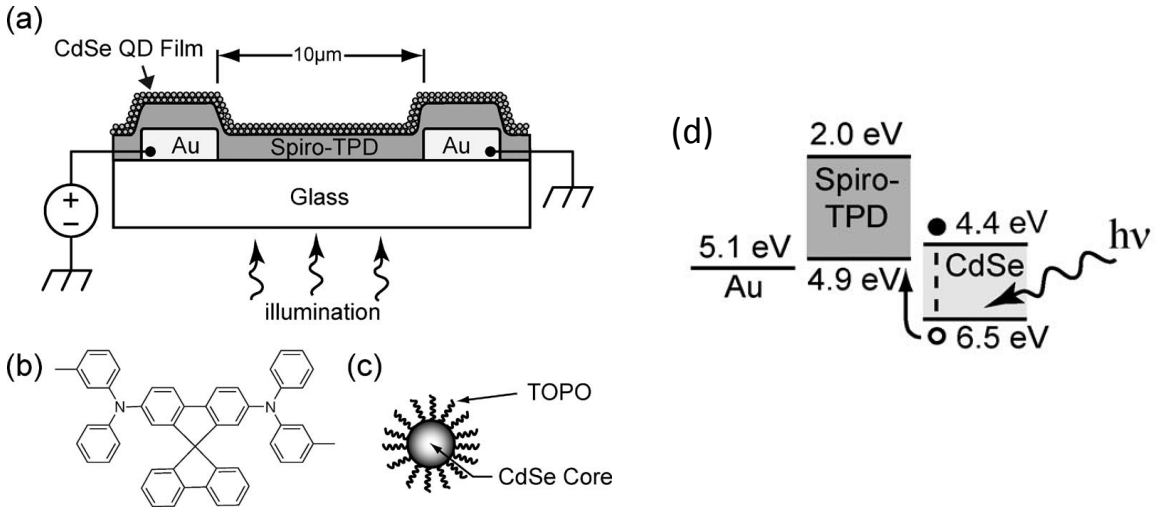

Figure 1.22: (a) Section view of the hybrid lateral OPD. The thickness of the spiro-TPD layer is 200 nm. The Au layer is 50 nm thick. The channel length is 10 µm. (b) Chemical structure of the hole-transporting material, spiro-TPD. (c) Schematic of CdSe nanocrystal passivated with TOPO ligands. (d) Energy structure of the lateral hybrid OPD [54].

Moreover, *T. P. Osedach et al*. (2010) [55] demonstrated then that using a hybrid HJ is advantageous in terms of speed of operation in comparison to an only-QDs based photodetector. Indeed, despite the high detectivity of QDs-based PDs, their use is limited due to their slow temporal response attributed to long-live QD surface trapping. Using a hybrid HJ made of a QDs layer and an organic semiconductor layer, although decreasing the sensitivity, accelerates the carrier recombination at the QD-organic interface and thus the response time. There is therefore a tradeoff between high sensitivity and temporal response.

Chapter 2: Thesis Organization

2.1. **Rationale**

The literature findings about lateral OPDs were discussed above. Despite this, the factors governing their photo-response are still not well understood. As charge carriers travel much longer distances in these devices in comparison to their more conventional vertical counterparts (10's of microns versus 10's of nanometers, respectively), both I_{ph} and I_d, and thus OPD sensitivity, can be expected to be influenced by additional factors, such as space charge build-up across the gap, a factor that has not been addressed. Moreover, it has been assumed, but never been verified, that the photocurrent arises from the dissociation of excitons created in the channel area only. Such a hypothesis could lead to a miscalculation of the device's quantum efficiency by omitting the contribution of the excitons generated outside of the gap area.

Furthermore, all lateral OPDs reported to date utilized a bottom contact architecture [51-56]. This is due to the need to keep the gap small which is often achieved by utilizing a lithography step in fabricating the contacts. As the organic materials generally have poor resistance to lithographic etching, the contacts must be fabricated first (on a substrate), prior to the deposition of the organic semiconductor layers. Nevertheless, a bottom contact architecture can be expected to lead to serious reliability and durability limitations. Indeed, in this architecture, the organic semiconductor layers, which are generally the most fragile and ambient-sensitive materials in the device, are situated above the metal contacts, and thus are afforded little protection. Moreover, a top-contact architecture could be expected to lead to a more uniform channel compared to the

bottom-contact one, due to the absence of "steps" at the metal-organic contact that could create significant non-uniformities due to shadow effects, especially for thin active layers [57]. Since the photocurrent mostly arises from the drift of the photogenerated carriers across the channel due to an external bias, a uniform channel is needed in order to improve the charge collection. Therefore, a top contact architecture is generally more desirable for practical applications. This is not unlike the case of OTFTs where a top contact architecture is more preferable.

In this work, a top contact lateral OPD fabricated through a simple shadow mask technique is introduced. A 25μm-wide gap between the two electrodes is created by utilizing a 25μm-diameter metal wire as a shadow mask during the metal deposition step. This work focuses on the physics of top-contact lateral OPDs.

2.2. **Objectives**

This work focuses on the following objectives:

(i) Developing a thermal evaporation-only fabrication process of top-contact lateral OPDs.

(ii) Understanding the factors governing both the dark and photo-currents of lateral OPDs.

(iii) Verifying whether the excitons generated outside of the gap area under bottom illumination contribute to the photoresponse.

(iv) Exploring the cycling stability of both dark and photo-current values for lateral OPDs under repeated operation cycles and under prolonged exposure to light.

(v) Estimating the external quantum efficiency of deep ultraviolet lateral OPDs using appropriate donor-acceptor systems and comparing their performances with reported vertical structures.

2.3. Approach and Methodology

This work utilizes small-molecule top-contact OPDs for all experiments. We use a device fabrication process only based on thermal evaporation. N,N′-di(naphthalene-1-yl)-N,N′-diphenyl-benzidine (NPB), Tris(8-hydroxyquinoline) aluminum (AlQ_3), and Ag are mainly used as the donor, acceptor, and electrodes materials, respectively. These constituent materials are chosen as they are established in literature as materials capable of producing efficient OPDs and have been extensively used in organic electronics.

The methodology of the work is as below:

(i) Fabrication of top-contact lateral OPDs using thermal evaporation. The configuration of the active layers is investigated and optimized.

(ii) Current-Voltage measurements taken under both dark and illuminated conditions. The effects of the measurements' parameters (scan direction, sweep rate, illumination direction, etc.) are investigated.

2.4. Structure of the thesis

This thesis consists of eight chapters.

Chapter one consists of an introduction to organic semiconductors; an overview of OPDs basic working principle and figures of merit; operational physics of OPDs including light

absorption, exciton formation and dissociation, and free carriers collection; followed by advances in OPDs; and concluding with an literature review of lateral OPDs.

Chapter two is related to the thesis organization, including the objectives, the methodology, and the structure of the thesis.

Chapter three is dedicated to the experimental methods involving, substrate preparation, the organic materials selection, device fabrication process, device testing.

Chapter four discusses the effects governing both the dark and photo-currents of top-contact lateral OPDs. Performances of the devices are systematically investigated by current-voltage measurements under dark and illuminated conditions.

Chapter five explores the reproducibility of both dark and photo-current under repeated operation cycles.

Chapter six provides external quantum efficiency and detectivity estimates of deep ultraviolet lateral OPDs using appropriate donor-acceptor combinations and benchmarks with reported vertical deep ultraviolet OPDs.

Chapter seven investigates the use of a phosphorescent sensitizer doped in the absorbing bottom layer to improve top-contact lateral OPDs efficiency.

Chapter eight provides conclusions of the experimental works seen in chapters four to seven, and recommendations for future work.

Chapter 3: Experimental Methods

Experimental methods involve the fabrication and testing of lateral OPDs. In this chapter, the fabrication of lateral OPDS is first introduced starting with the substrate preparation and ending with material deposition. After that, measurement equipment and techniques used to characterize lateral OPDs are introduced.

3.1. Fabrication of lateral OPDs

3.1.1. *Substrate preparation*

Two different types of substrates are used for the fabrication of lateral OPDs: pre-patterned Indium Tin Oxide (ITO) on polished soda lime glass (15Ω/sq) and bare quartz substrates as displayed in *Figure3.1*.

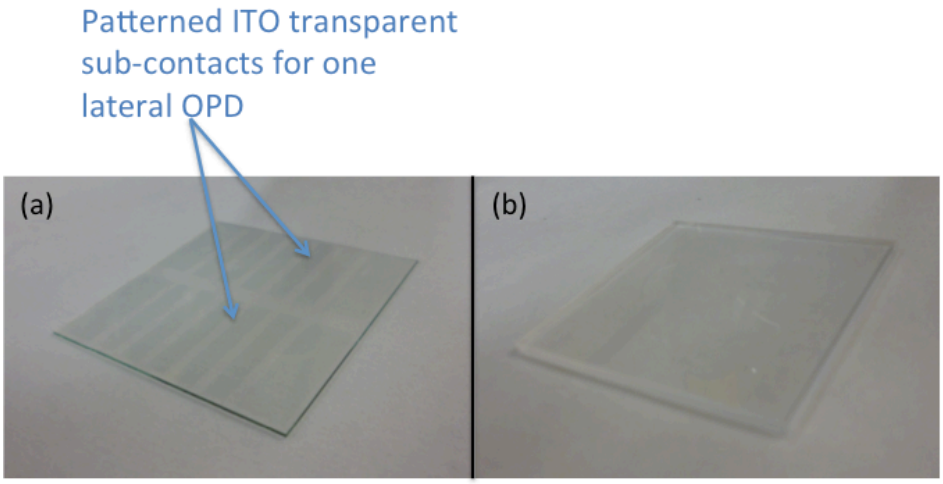

Figure 3.1: (a) Pre-patterned ITO on glass and (b) neat quartz substrates.

Quartz substrates made of fused silica are used for deep ultraviolet violet (wavelengths below 350nm) detection under bottom illumination since they are almost completely transparent in this range of the electromagnetic spectrum in contrast to standard glass substrates, as shown in *Figure 3.2*. The bare quartz substrates used need however to be patterned before the evaporation of the active layers in order to create

metallic sub-contacts necessary for the post-fabrication characterization. Thermal evaporation is used for the patterning.

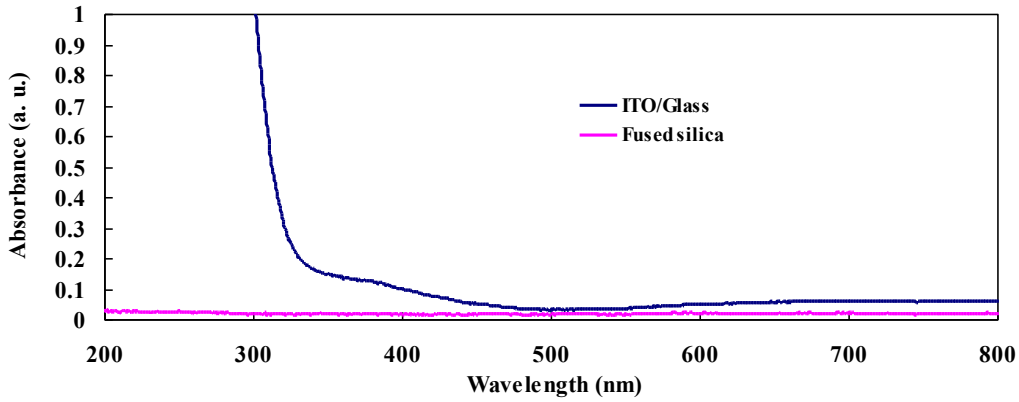

Figure 3.2: Absorption spectra of ITO/Glass and fused silica**.**

The cleaning process is the same for both types of substrates:

(i) The substrate is submerged into a 1L beaker with 500mL of acetone and washed in an ultrasonic bath for 15 minutes to remove all kinds of organic contaminations on the substrate's surface.

(ii) The substrate is rubbed gently with Q-tips to remove any contaminations sticking on the surface.

(iii) The substrate is then submerged in 500mL of isopropanol and is subjected to another 15 minutes ultrasonic wash.

(iv) A nitrogen gun is used to dry the substrate after the ultrasonic washing and blow away any extra solution on the substrate surface.

(v) Finally, the substrate is baked in an oven for 125°C for 30mins for further drying.

3.1.2. *Plasma treatment of ITO/glass substrates*

Before the device fabrication on ITO/Glass substrates, further cleaning of the ITO surface by using reactive ion etching (RIE) technology is conducted. This is because RIE applies plasma treatment to the ITO reducing its work function [58] and improving the general stability of the devices (based on experimental and unpublished conclusions). The optimal parameters of RIE for substrate treatment are listed in *Table 3.1*

Parameter	Value
Pressure	20 mTorr
Inductively Couple Plasma Power	100 Watts
Duration	2 min
Gas proportions	CF_4 (75%): O_2 (25%)
Gas rates	CF_4 (15sccm): O_2 (5sccm)

Table 3.1: Plasma treatment of ITO/Glass substrates parameters.

3.1.3. *Thin Film Deposition by Physical Vapor Deposition (PVD)*

3.1.3.1. PVD equipment

The organic films are deposited by PVD using the Angstrom EVOVAC Deposition system. This machine is capable of combining multiple thin film deposition sources, using up to ten thermal evaporation sources, electron beam evaporation, and four magnetron sputtering target, in the same chamber. In this work, all the organic material thin films were fabricated only using the thermal evaporation sources of the Angstrom EVOVAC Deposition system. The 10 thermal evaporation sources are controlled by 4 outputs and are monitored by 4 crystal sensors and it is consequently possible to mix up to 4 different materials by co-evaporation.

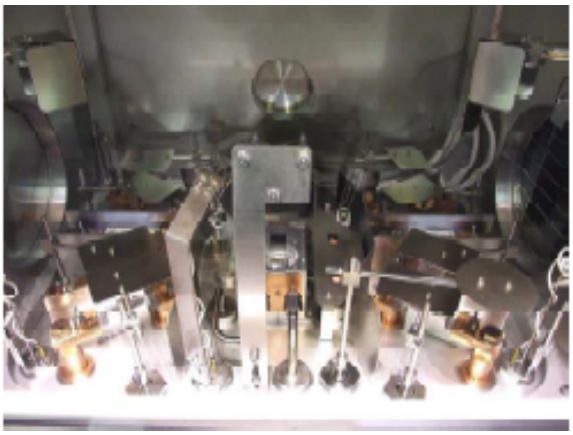

Figure 3.3: Angstrom EVOVAC Deposition system.

3.1.3.2. Materials used

In this work, most devices were fabricated utilizing N, N'-Bis(naphthalen-1-yl)-N,N'-bis(phenyl)-benzidine (NPB) and tris(8-hydroxyquinolinato) aluminum (AlQ3) as a light absorbing donor material and electron acceptor material, respectively. NPB has strong absorption at 350 nm, and the heterojunction at the NPB/AlQ3 interface is known to be efficient in the dissociation of excitons formed in the NPB layer [59], thus the materials can serve as good model compounds for materials typically used in UV OPDs. 1,3,5-tris(3- methylphenyl-phenylamino) triphenylamine (m-MTDATA), bathophenanthroline (BPhen), bis(2-methyl-8-quinolinolato-N1,O8)-(1,1'-Biphenyl-4-olato)aluminum (BAlQ), and fullerene C_{60} were also used. Similarly, Ag is principally used for the deposition of the contacts. Al and Mg:Ag (9:1 ratio) contacts have also been investigated. The molecular structures of the organic molecules, their HOMO and LUMO levels, as well as the work functions of the metal used are displayed in *Figure 3.4*. Specific device structures are described in the corresponding chapters of this thesis.

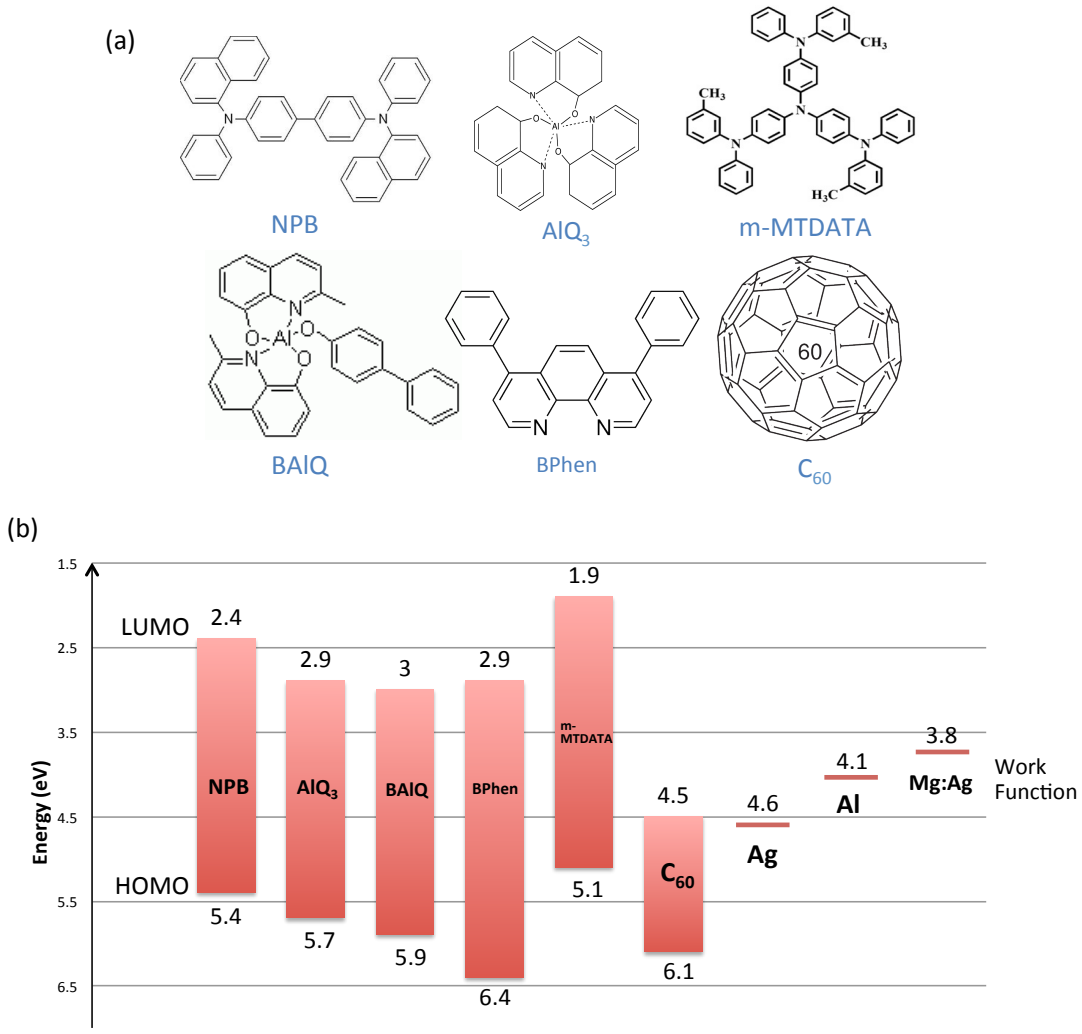

Figure 3.4: (a) Molecular structures of the organic molecules used in this thesis and (b) their HOMO and LUMO levels. The work functions of the metals used are also indicated.

3.1.3.3. Deposition parameters

The top contact lateral OPDs are entirely fabricated by thermal evaporation of the organic materials and metal contacts at vacuum base pressure of about 5.10^{-6} Torr on cleaned substrates. The rate of deposition is $1 Å/s$ for both organic materials and metals.

3.1.3.4. Fabrication process of top-contact lateral OPDs

The fabrication process of lateral OPDs can be divided in 5 basic steps:

(i) Patterning of the cleaned quartz substrates by deposition of Ag through a metallic shadow mask (this step is absent in case of fabrication on ITO/glass substrates);

(ii) Deposition of the organic layers through a very thin (a few micrometers thick) plastic shadow mask to avoid shadow effects;

(iii) The metallic wire (diameter $\sim 25\mu m$) is tightly taped on top of the organic layers**;**

(iv) Deposition of Ag through a different plastic shadow mask allowing to obtain 5 different devices on a single substrate;

(v) Removal of the wire to create the two contacts separated by a gap of $\sim 25\mu m$. The width of the gap between the two contacts is usually $\sim 25\mu m$ but can be varied in case of specific structure using metallic wires of $\sim 35\mu m$ and $\sim 50\mu m$. The length and width of the active layers are 1.9cm and 4mm, respectively.

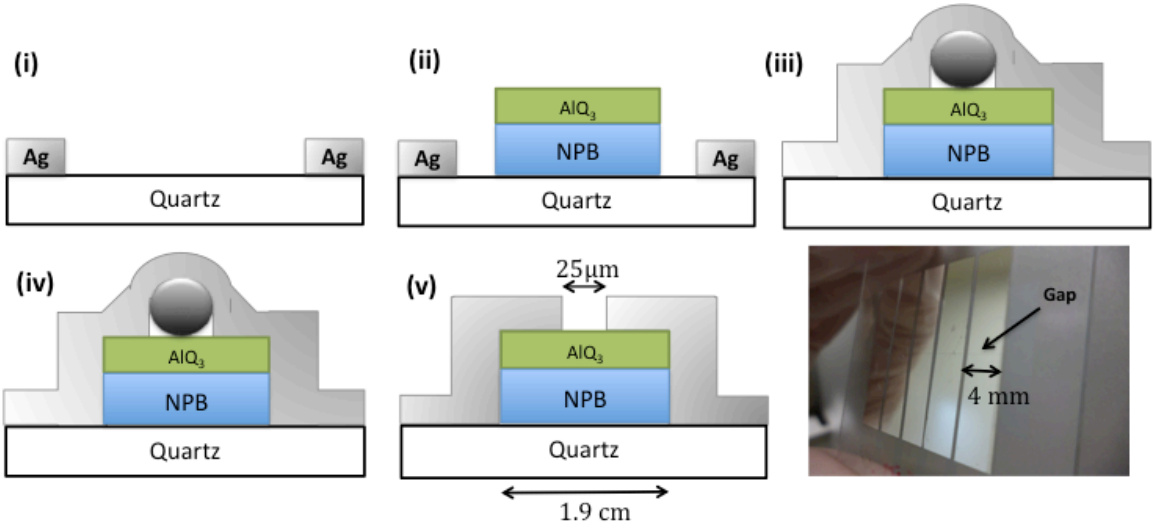

Figure 3.5: Fabrication process of top-contact lateral OPDs.

3.1.3.5. Encapsulation of lateral OPDs

When specified in the thesis, the top-contact lateral OPDs are encapsulated using a piece of glass glued on top of the metallic contacts with epoxy.

3.2. **Testing of lateral OPDs**

After the device fabrication, all the testing and measurements of OLEDs are carried out in a nitrogen atmosphere and at room temperature. During the testing, devices are installed in testing box with nitrogen flowing through to prevent the ambient degradation. Between different testing, the devices are also stored in a metal storage box.

3.2.1. *Current-Voltage characteristics*

Current-voltage (I-V) measurements are carried out using an Agilent 4155C semiconductor parameter analyser (*Figure 3.6)*.

Figure 3.6: Agilent 4155C semiconcdutor parameter analyser.

The dark current measurements are performed while the sample is kept in the dark. Photo-measurements are performed using a 200 W Hg–Xe white lamp equipped with Oriel-77200 monochromator, with the sample illuminated from the bottom (i.e. through the substrate). The setup is shown in *Figure 3.7.* In general, the photocurrent measurements were carried out at a wavelength of 350nm.

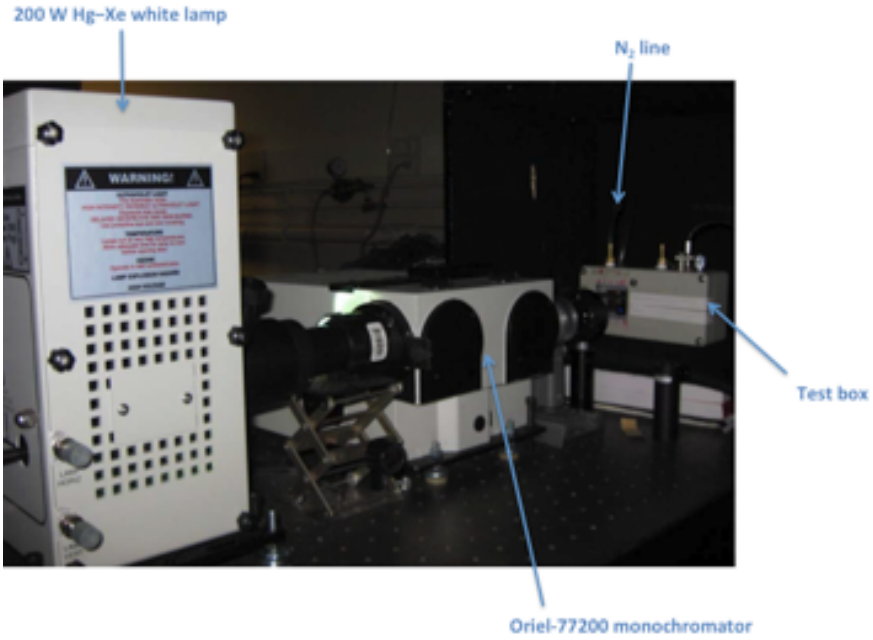

Figure 3.7: Photo-current measurement setup.

3.2.2. *Absorption and transmittance spectra*

The optical absorption and transmittance spectra are measured by using a Shimadzu UV-2501PC UV-Visible spectrophotometer.

Chapter 4: Factors governing the dark and photo-currents of top contact lateral organic photodetectors

In this chapter we studied the dependences of both I_d and I_{ph} of top-contact lateral OPDs.

Figure 4.1 shows the I-V characteristics, both in the dark (dashed lines) and under UV illumination (0.8mW/cm^2 at 350nm) (solid lines), of a bilayer heterojunction lateral OPD, comprising a 50nm-thick NPB layer and a 20nm-thick AlQ_3. The figure inset shows the same data, but presented as a function of the bias electric field, calculated assuming the electric field is uniform in the channel. This is provided here only to allow approximate comparisons with other published data. As, in principle, the electric field will not be uniform [60], we revert to the use of voltages rather than electric fields throughout the rest of this work in the interest of accuracy. As the figure shows, the device exhibits a good photo-response, reflected in a substantially higher current flow under illumination versus that in the dark. For example, the I_{ph}/I_d ratio at 15V bias is about 100 times. It is noticed that I_d and I_{ph} show different dependences on the applied voltage suggesting they may be governed by distinct phenomena. In general, increasing the bias would be expected to increase both I_{ph} and I_d; the earlier due to an increase in exciton dissociation and charge collection, and the latter due to an increase in injection from the contacts. A close examination of the figure however reveals that, although increasing the bias leads to a significant increase in I_{ph} over the entire range of voltage, the increase in I_d with voltage is observed to be limited only to the initial part (up to ~1.5V), after which the trend quickly saturates, and I_d becomes essentially insensitive to further increases in voltage. This suggests that I_d is limited by charge injection from the contacts only initially (i.e. $V < \pm 1V$) but becomes limited by other phenomena, likely

associated with the very limited conduction across the gap in the dark at high voltages. A close examination of the I_d also reveals a small "negative resistance" effect in the 2-3V voltage range, where the current slightly decreases as the voltage increases. Besides, the I_d and I_{ph} trends were very similar for both the positive and the negative bias, which is not unexpected given the symmetric device geometry. It should be noted however that these characteristics are obtained through two separate I-V scans; one scan from 0V to 15V and the other from 0V to -15V. We found that starting the I-V scan at a non-zero voltage alters the shape of the trend, and, in general, leads to asymmetric characteristics

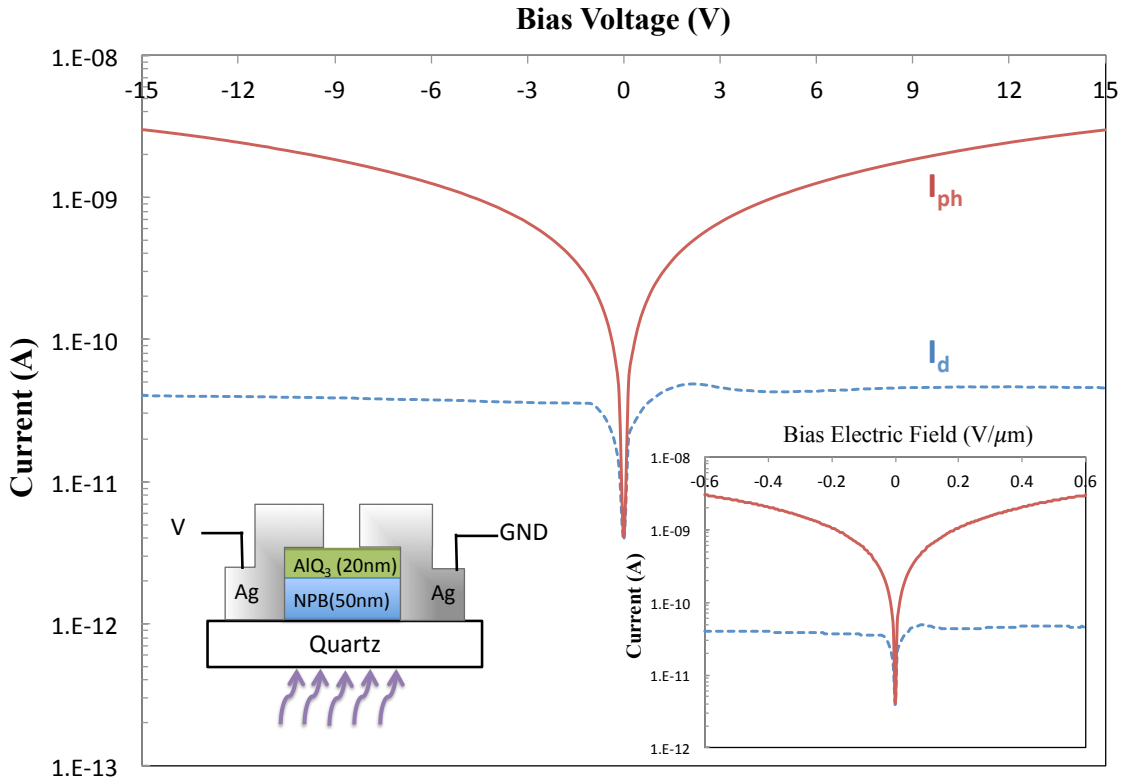

Figure 4.1: Semi-logarithmic plot of the basic current-voltage (I-V) characteristics of a top contact lateral OPD using NPB as donor (50nm) and AlQ_3 as acceptor (20nm) materials. Both dark current (I_d, dashed lines) and photocurrent (I_{ph}, solid lines) are plotted on the same graph. I_{ph} is obtained under bottom illumination at a wavelength of 350nm and power density of 0.8mW/cm^2. For both I_d and I_{ph}, two I-V separate scans are performed and combined: (i) from 0V to 15V (ii) from 0V to -15V. The inset shows the evolutions of I_d and I_{ph} as a function of the electric field across the gap, assuming the electric field is uniform across the channel

Figure 4.2(a) shows I-V data collected from the same device using 3 different scan scenarios; (i) from -15V to 15V, (ii) from 15V to -15V, and (iii) using two separate I-V scans; one scan from 0V to 15V and the other from 0V to -15V. Clearly, starting the scan at -15V or 15V instead of 0V leads to highly asymmetric I_d trends, causing the minimum-current point to occur at a negative or a positive voltage, respectively, instead of zero. Furthermore, the I_d level at the beginning of the scan (i.e. I_d at -15V in case of (i), and at 15V in case of (ii)) is remarkably higher than that in case of (iii) at the same voltage. This high initial I_d decreases rapidly as the scan proceeds however, and the I_d level becomes comparable to that in case of (iii). It is also noticed that the I_d trace is generally steeper in the first part of the scan, but, remains relatively horizontal (i.e. varies only negligibly with bias) in the latter part of the scan. Despite the asymmetry in the I_d trends of each of (i) and (ii), the two trends are essentially mirror images of each other, with minimum-current points at ~-4V and ~4V respectively, indicating that the asymmetry is caused entirely by the sweep direction. On the other hand, and in sharp contrast to the case of I_d, the I_{ph} trends are not strongly affected by the scan direction, and remain essentially symmetric with a minimum-current point at ~ 0V for all test scenarios.

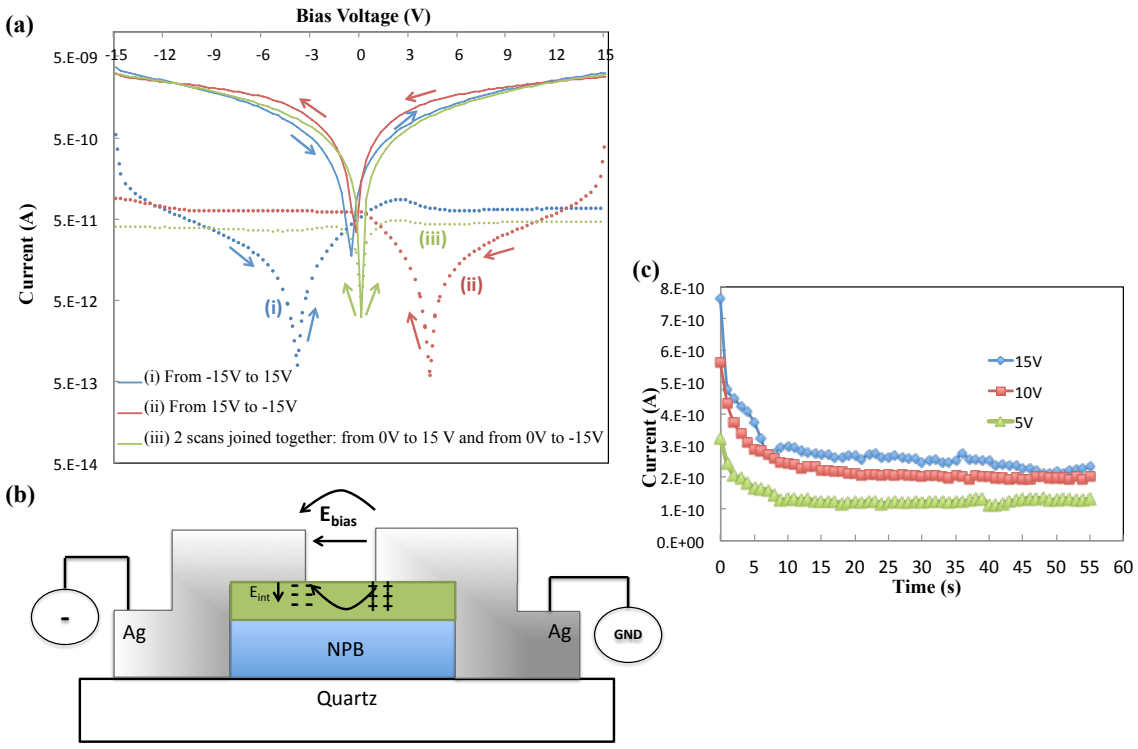

Figure 4.2: (a) I-V characteristics obtained for different scan scenarios: (i) from - 15V to 15V ; (ii) from 15V to -15V ; (iii) from two separate scans : from 0V to 15V and from 0V to -15V. The arrows are guides to eyes to indicate the scan direction. (b) Schematic of the charge accumulation in the AlQ_3 top layer near the contacts. (c) Evolution of I_d with time at 3 constant biases: 15V, 10V, and 5V.

Because in lateral OPDs the gap size is much larger in comparison to the layers thickness (microns vs nanometers, respectively), conduction between the electrodes, and hence also the shape of the I-V trend, is predominantly limited by conduction across the gap. The different dependence of I_d and I_{ph} on the scan direction therefore reflects differences in conduction across the gap under illumination versus in the dark. The fast decrease in I_d that occurs in the beginning of the scan in case of (i) and (ii) suggests the rapid formation of space charges in the organic layers, most likely in the AlQ_3 layer, near the edges of the metallic contacts as soon as carriers are first injected into it. These accumulated charges create an internal electric field, E_{int}, near the contacts, opposite to that produced by the external bias which quickly limits further charge injection. The rapid formation of space charges can be attributed to the very poor conduction across the

gap due to the low electron mobility in AlQ_3 (~ $10^{-5}cm^2/V.s$) and the very low carrier concentration in the dark, which seriously limits the transport, and hence the dissipation, of the injected charges. *Figure 4.2(b)* illustrates this effect for the case of scenario (i). As the magnitude of the external bias is gradually decreased, some of these accumulated charges can drift back towards the electrode from which they were injected under the effect of E_{int}, and hence the non-zero minimum-current point (-4V in case of (i)). Starting the I-V scan at 0V and gradually increasing the magnitude of the bias (i.e. scenario (iii)) would similarly lead to the formation of space charges near the contacts. But as in this case the magnitude of the applied field continuously increases (i.e. does not initially decrease as in case of (i) and (ii)), the magnitude of E_{int} never exceeds that produced by the external bias. Therefore, the accumulated charges cannot drift back towards the electrodes in this case, and thus the minimum-current point appears at 0V. Obviously, any current flow across the gap in the bias direction requires that the bias field must first exceed E_{int}. The fact that I_d eventually "plateaus" and does not continue to increase with bias in the last part of the scan in all 3 scenarios suggests that conduction across the gap continues to be very low, a sign that it continues to be essentially depleted of carriers, even at these relatively high bias voltages. Therefore it is likely that I_d arises mostly from transient capacitive currents due to the accumulation of charges near the contacts. The component of I_d arising from the steady-state drift of carriers across the gap is much smaller in comparison, and is perhaps significant only at high bias voltages. *Figure 4.2(c)* displays the evolution of I_d as a function of time under constant bias (15V, 10V or 5V). Clearly, the figure shows a fast decrease in I_d in the first few seconds (<10s) consistent with transient capacitive charging effects, and then the current becomes almost constant

at a lower value (~ 40% lower than the initial value) which might correspond to the small drift current component across the channel. This perhaps explains the remarkably low dark current levels in lateral OPDs over a relatively wide bias range. We can therefore conclude that, except at very low bias levels (<±~2V) where current is limited by injection from the contacts, I_d in lateral OPDs is primarily limited by space charge limited conduction (SCLC) across a highly depleted (i.e. essentially insulating) gap, and is dominated by capacitive transients. The I_{ph} characteristics, on the other hand, remain essentially symmetric regardless of the scan direction which therefore suggests the formation of a conductive "channel" for charge transport across the gap only when under illumination. The formation of this channel across the otherwise depleted gap becomes possible due to the much higher carrier concentration as a result of photogeneration. Thanks to the much easier charge transport across the gap, space charge effects become much less, and hence the insignificant effect of altering the scan direction on I_{ph}. All the I-V characteristics introduced in the rest of this study are obtained by scans conducted in the direction -15V → 15V (scenario (i)).

Seeing that device characteristics are strongly influenced by SCLC effects, the effect of changing the I-V scan rate on I_d and I_{ph} is also investigated. Decreasing the scan rate (i.e. reducing the total time it takes to complete a scan) can be expected to reduce space charge effects as a result of the lower total number of charges that get injected into the organic layers during the entire scan. *Figure 4.3* shows the I-V characteristics of one device collected at various scan rates. In all cases, the scan was conducted in the direction -15V → 15V as mentioned above. As observable in *Figure 4.3 (a)* increasing the sweep rate (i.e. decreasing the sweep time) leads to a significant increase in I_d, which is

consistent with a lower density of space charges that limit I_d. Here again, as can be seen from *Figure 4.3 (b)*, the photocurrent is not significantly affected by the change in the sweep rate. This is due to the high concentration of photo-generated carriers in the gap, which enhance conduction, thus minimizes the formation of space charges.

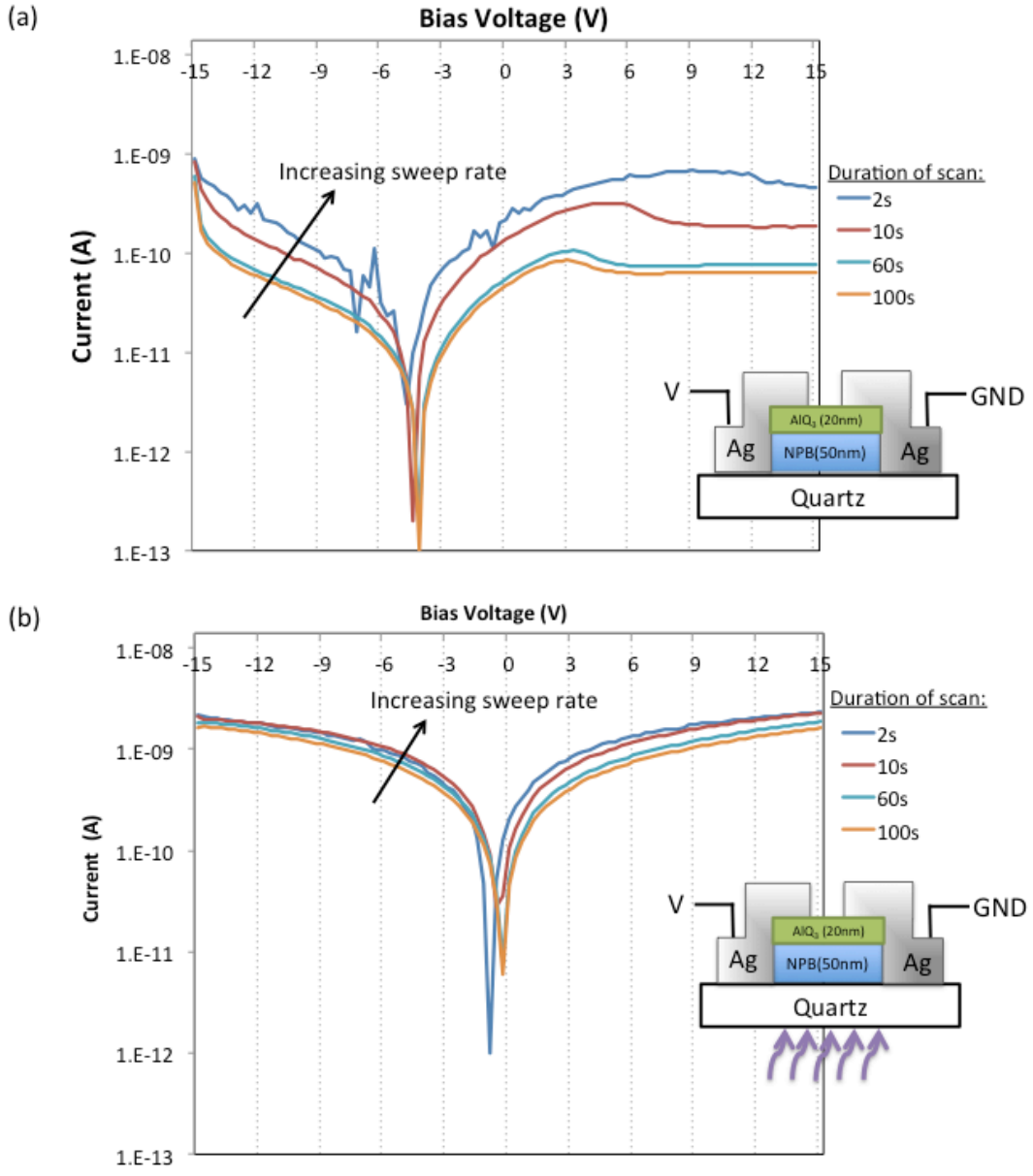

Figure 4.3: Effect of scan duration on both (a) I_d and (b) I_{ph}.

Similarly, the influence of the nature of the metallic contacts on I_d is explored. *Figure 4.4* compares I_d of devices with identical structures except the metal used for the two lateral contacts is varied between Ag, Al and Mg:Ag (9:1) that show work function of 4.6eV, 4.1eV, and 3.8eV, respectively. From the figure, it is observable that the device using lower work function Mg:Ag contacts exhibits a highly asymmetric I_d, the minimum-current point occurring at ~ -4.5V, while the devices using higher work functions Al and Ag contacts present less asymmetric I_d with a minimum-current point occurring at ~ -4V and ~ -3.5V, respectively. The steep drop in I_d at the beginning of the scan is also more pronounced when the work function of the metal is decreased. This evolution of I_d while decreasing the work function of the contacts is attributed to a higher electron injection at the beginning of the scan that leads to an increase in the concentration of space charges near the edges of the metallic contacts. The minimum-current point occurs thus at higher voltages since the value of E_{int} is increased.

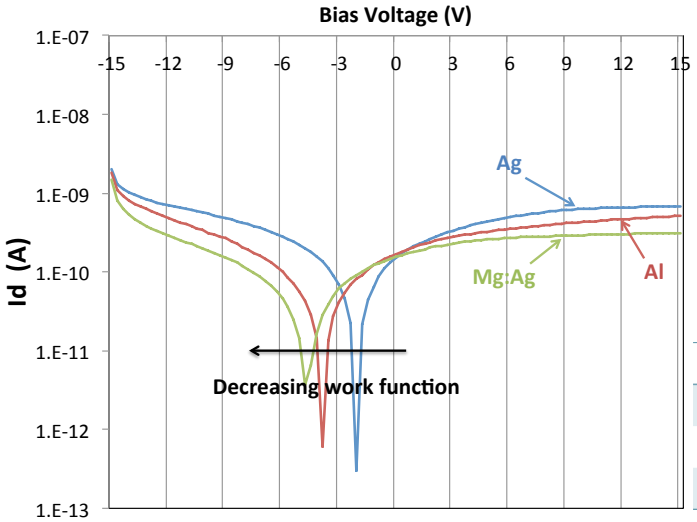

Metal	Work Function (eV)
Ag	4.6
Al	4.1
Mg:Ag (9:1)	3.8

Figure 4.4: Effect of the metal contacts work functions on I_d.

These conclusions are confirmed when studying the effect of the gap size, i.e. of the channel width, on both I_d and I_{ph}. Using shadow mask wires of different diameters enabled to design lateral OPDs with 3 different gap sizes: 25µm, 35µm, and 50µm. Both I_d (*Figure 4.5.(a)*) and I_{ph} (*Figure 4.5.(b*)) were compared and plotted first as a function of the applied voltage and second as a function of the lateral electric field across the gap, which was obtained by dividing the applied voltage by the gap size for each of the 3 devices, assuming the electric field is uniform across the channel. As can be seen in *Figure 4.5(a),* the minimum current point of the three devices appears at the same bias value as opposed to the same gap electric field value, indicating that the drift of carriers across the gap under the electric field produced by the bias indeed does not contribute significantly to I_d (otherwise the current would have shown a stronger correlation with the electric field across the gap), consistent with the conclusion that I_d arises mostly from displacement currents produced by the motion of charges between the contacts and the organic layers below them (i.e. charging effect). On the other hand, *Figure 4.5(b)* demonstrates that I_{ph} in lateral OPDs mostly comes from the conduction of the photogenerated carriers through the illuminated channel since I_{ph} of the 3 different gap sizes devices match when plotted as a function of the lateral electric field. It is therefore believed that, in the case of lateral OPDs, an external illumination provides enough photogenerated carriers to overcome the SCLC effects limiting the conduction in the dark, making the channel area the main active area for the photoresponse.

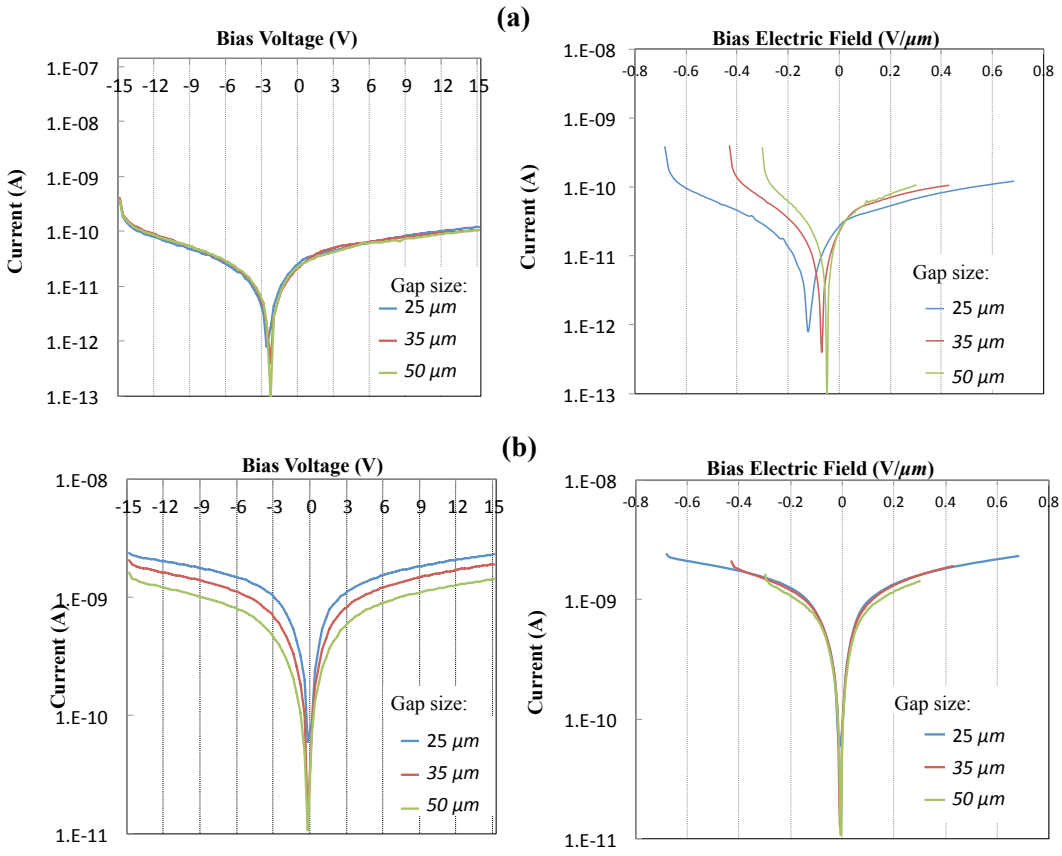

Figure 4.5 (a) I_d plotted as a function of the applied voltage (right hand side corner) and as a function of the electric field (left hand side corner), assuming the electric field is uniform across the channel for, for 3 different gap sizes: 25μm, 35μm and 50μm. (b) I_{ph} plotted as a function of the applied voltage (right hand side corner) and as a function of the electric field (left hand side corner), assuming the electric field is uniform across the channel for, for 3 different gap sizes: 25μm, 35μm and 50μm.

Moreover, in order to optimize the lateral OPDs' performances, it is important to identify how the photogenerated carriers are created and which configuration of the organic layers is the most suitable. *Figure 4.6(i)* shows the values of I_{ph} taken at a voltage bias of 8V for five lateral OPDs with different organic layer configurations (a) NPB(50nm)/AlQ3(20nm)/Contacts; (b) NPB(20nm)/AlQ3(50nm)/Contacts; (c) AlQ3(20nm)/NPB(50nm)/Contacts; (d) NPB(50nm)/Contacts; and (e) NPB:AlQ_3 (1:1) mixture (70nm)/Contacts to investigate the effect of the interfaces density on the photoresponse. In device (a), the I_{ph} arises from photo-generated carriers produced from

excitons created in the thick NPB light-absorbing layer. A fraction of these excitons diffuses to the NPB/AlQ_3 interface where, due to the HOMO and LUMO offsets of NPB and AlQ_3 [59], they get dissociated into "free" electrons and holes on AlQ_3 and NPB molecules, respectively, across the interface. The electrons are collected through the AlQ_3 acceptor layer, and drift across the gap under the effect of the applied bias towards the contact with the more positive potential. The holes are transported into the NPB layer towards the opposite electrode and subsequently cross the thin AlQ_3 layer to be collected by the contact. Compared to the standard photoresponse of device (a), device (b) exhibits a very low I_{ph}. This absence of photoresponse is likely to be due to the lower absorption of AlQ_3 at 350nm in comparison to NPB, as shown in *Figure 4.6(ii)*. Not enough excitons are created in the AlQ_3 absorbing layer to provide free carriers after their dissociation at the organic-organic interface. The very low I_{ph} could be due instead to the dissociation of the few excitons created in the thin top NPB layer. Device (c) demonstrates better performances than device (b) but still exhibits a lower I_{ph} than the optimized device (a). As the very thin AlQ_3 bottom layer (only 20nm) exhibits limited absorption at 350nm, the majority of pa photons are absorbed in the top 50nm thick NPB layer. The excitons created in the NPB layer are dissociated at the interface with AlQ_3 into free holes and electrons with an efficiency that should be similar to the one of device (a). However, the free carriers have to eventually cross the thick top NPB layer and the collection is reduced due to charge trapping of carriers before they reach the metallic contacts. Although being lower compared to both device (a) and (c), I_{ph} of device (d), without any dissociative interface, remains significant and suggests that lateral OPDs efficiencies are predominantly limited by carrier collection more than by exciton dissociation. The low

I_{ph} of device (e) confirms that I_{ph} strongly depends on the transport of the carriers to the contacts since, event though the dissociation efficiency of the active layer is enhanced by a much higher NPB/AlQ_3 interfacial area (due to the mixing), the collection efficiency is reduced due to an increase of the charge trapping rate in the mixture [61]. The lower photoresponse compared to device (a) can also be attributed to a decrease in the absorption at 350nm when AlQ_3 acceptor molecules are inserted into the NPB matrix. Moreover, the electric field being low in lateral OPDs, increasing the number of interfaces could lead to a significant increase in the geminate recombination rate since excitons field-induced dissociation is likely to be reduced.

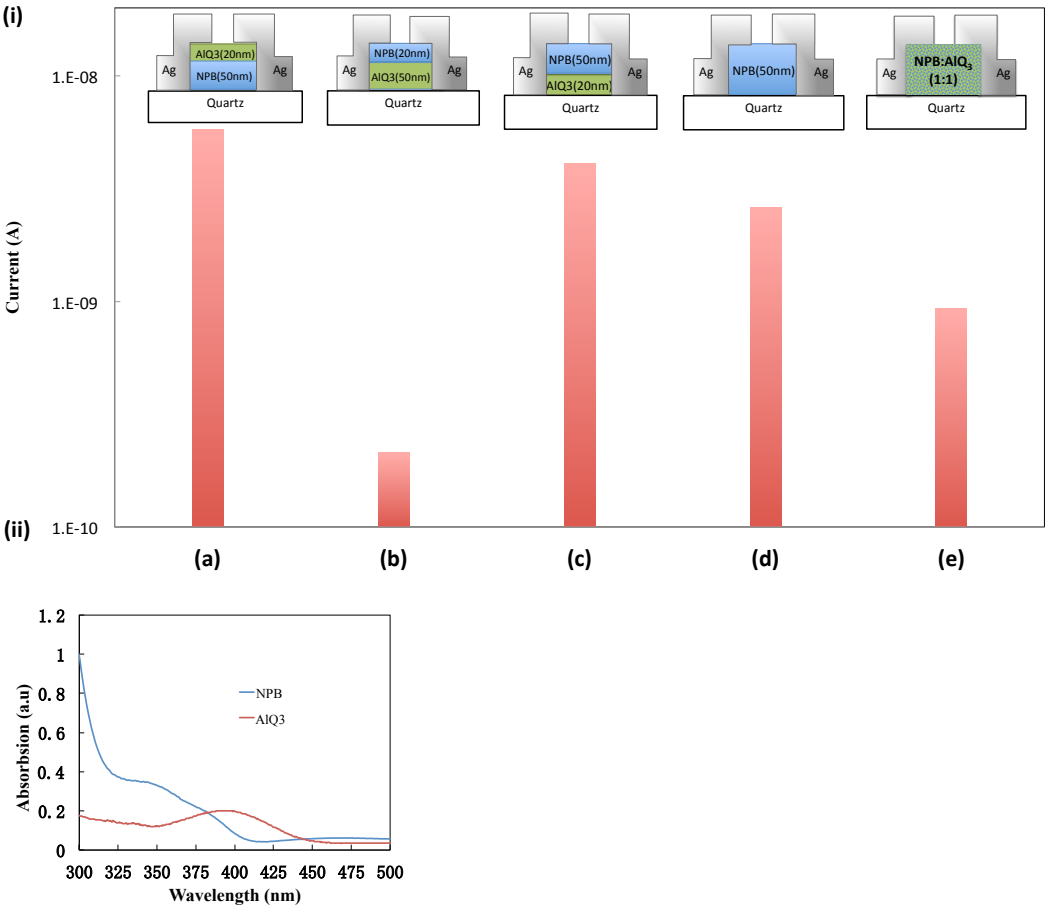

Figure 4.6: (i) Values of I_{ph} taken at a voltage bias of 8V for five lateral OPDs with different organic layer configurations (a) NPB(50nm)/AlQ3(20nm)/Contacts; (b) NPB(20nm)/AlQ3(50nm)/Contacts; (c) AlQ3(20nm)/NPB(50nm)/Contacts; (d) NPB(50nm)/Contacts; and (e) NPB:AlQ_3 (1:1) mixture (70nm)/Contacts (ii) UV-Vis of 40nm-thick pristine NPB and AlQ_3 films.

To further understand the electrical behavior of lateral OPDs, we investigated the effect of the organic layers thicknesses on both I_d and I_{ph}. *Figure 4.7(a)* shows normalized I_d values, taken at a bias voltage of 15V, as a function of NPB and AlQ_3 layers thicknesses. Two sets of devices were fabricated varying either NPB or AlQ_3 thicknesses: one in which the NPB thickness varies from 20 to 100nm while the AlQ_3 thickness is fixed at 20nm; another one in which the AlQ_3 varies from 5 to 50nm while the NPB absorbing layer thickness is fixed at 50nm. As can be observed from the figure, I_d does not seem to depend on both donor and acceptor layers' thicknesses since no distinct trend is observable. This suggests that the capacitive component of I_d is influenced by charge build-up in the organic layers only near the surface and not deep into the bulk. On the other hand, it is observable that I_{ph} depends on both NPB and AlQ_3 thicknesses as described in *Figure 4.7(b)*. A too thin (< 50nm) NPB layer seems to reduce the absorption of photons and therefore the creation of excitons that get dissociated at the NPB/AlQ_3 interface into free carriers. On the other hand, a too thick absorbing layer (>50nm) might decrease the photogeneration of free carriers since the fraction of excitons created in the first nanometers of the absorbing layer would recombine before reaching the dissociating interface, in accordance with a reported NPB excitons diffusion length of around 5nm [62]. Similarly, the photoresponse appears to depend on the acceptor layer thickness since an AlQ_3 thinner than 20nm could increase direct Forster excitons quenching at the metallic contacts (the Forster radius being comprised between 3nm and 10nm) and an AlQ_3 layer thicker than 20nm may promote charge trapping of free carriers dissociated at the NPB/AlQ_3 interface before collection at

the electrodes. The results of *Figure 4.7* therefore justify the use in this study of a 50nm thick NPB layer and a 20nm thick AlQ_3 layer.

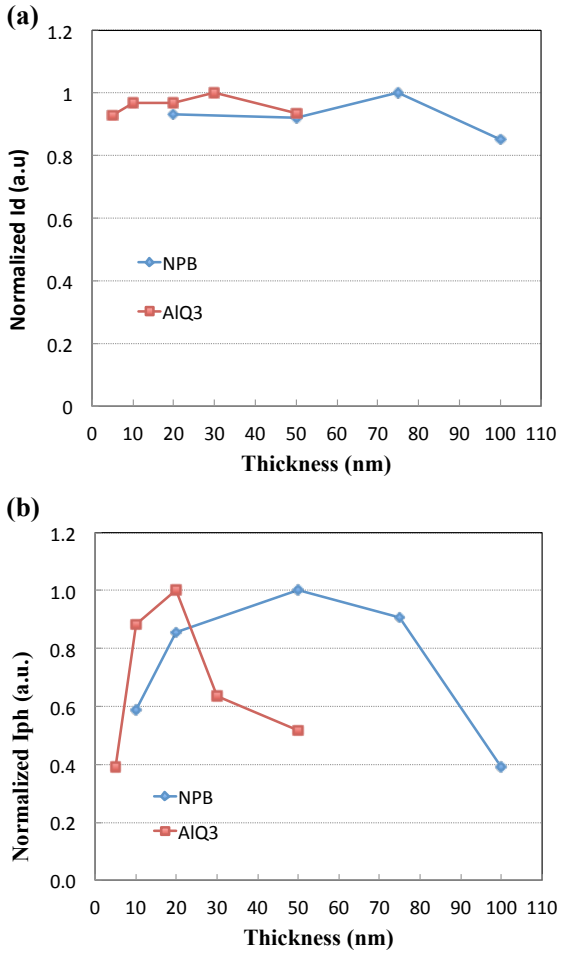

Figure 4.7 (a) Dependence of I_d and (b) I_{ph} on both NPB and AlQ_3 layers thicknesses. When the NPB layer thickness is varied, the AlQ_3 layer thickness is kept to 20nm. When the AlQ_3 layer thickness is varied, the NPB layer is kept to 50nm.

Seeing that I_{ph} is collection limited, we investigated the dependence of the acceptor layer mobility on the photoresponse by introducing 4,7-diphenyl-1,10-phenanthroline (BPhen) into the AlQ_3 layer. *Figure 4.8* shows the I-V characteristics of devices with different BPhen concentrations: (a) 0% (i.e. pristine AlQ_3 layer), (b) 20%, (c) 50%, and (d) 100% (i.e. pristine Bphen layer). It is observable that for devices (c) and (d) I_{ph} is increased compared to device (a) (increase of 68.4% at 6V in the case of device (d))

while I_d remains the same. Since the electron drift mobility of BPhen is about two orders of magnitude higher than the one of AlQ_3 [63], the increase in I_{ph} might be attributed to the improved mobility of the acceptor layer via electron hopping exchange from AlQ_3 molecules to BPhen molecules since their LUMO-LUMO (both around 3.0eV) difference is minor. A higher electron drift mobility leads to a faster collection of carriers at the contacts. Similar improvements in organic light-emitting diodes (OLEDs) efficiencies using a AlQ_3:BPhen high mobility electron transport layer have been reported and attributed to a good balance between hole and electron transports [64, 65]. Moreover, I_{ph} in the case of device (d) stays almost unchanged for voltages higher than $\pm$~6V while it keeps increasing with a steeper slope in the case of AlQ_3. The less steep trend with BPhen may perhaps be due to a smaller variation in its mobility with electric fields (according to the Pool Frenkel model [65]) in comparison to that of AlQ_3 possibly due to the closer intermolecular packing. This confirms the fact that I_{ph} is strongly charge-collection limited. The increase in I_{ph} could also be due to a better absorption of BPhen at 350nm than AlQ_3 which would create more photogenerated carriers. On the other hand, the similar I_d for each device confirms that I_d is much less governed by charge transport across the channel than by capacitive currents associated with the accumulation of charges near the contacts. It is noteworthy to point out that introducing only 20% of BPhen in the acceptor layer in the case of device (b) does not improve the device's photoresponse and leads to a decrease in I_{ph}. This might be attributed to a charge trapping effect in the top layer that counter-balances the improvement in the electron drift mobility. The electric field being much lower in lateral devices than in vertical ones and

the distances much longer, it is possible that charge trapping prevails on mobility enhancement at low BPhen concentrations.

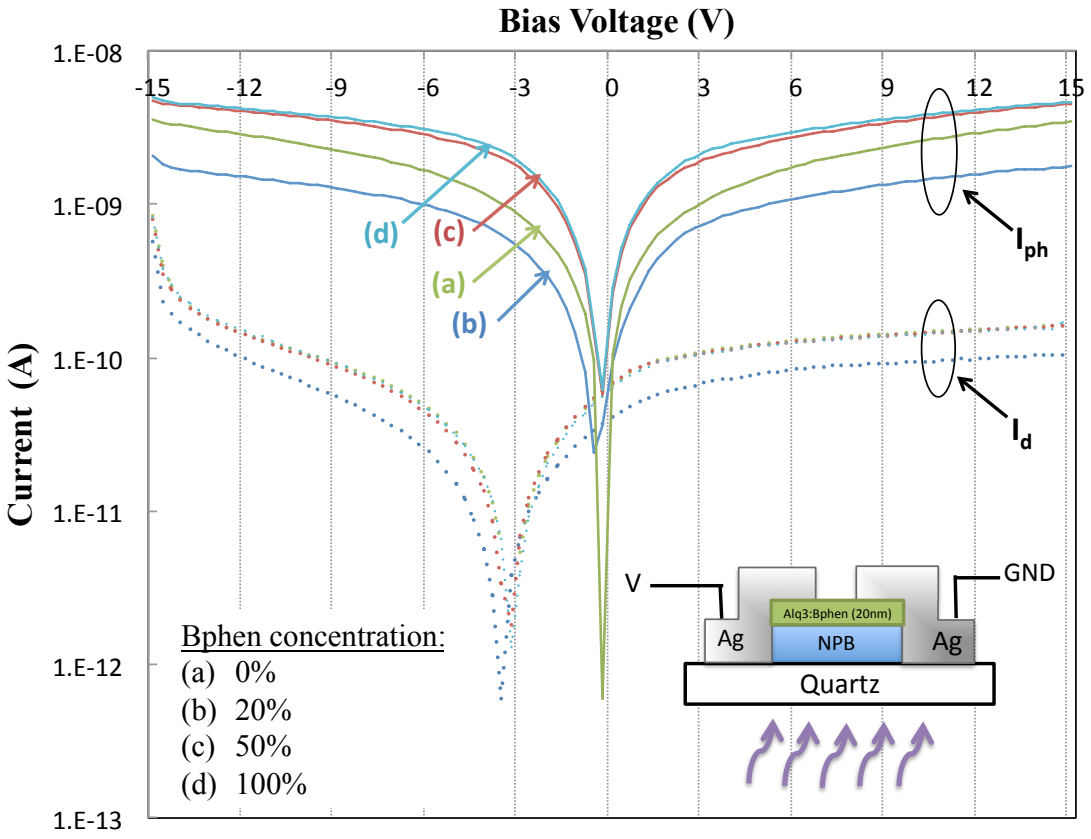

Figure 4.8: I_d (dashed lines) and I_{ph} (solid lines) of devices with different BPhen concentrations in a co-host AlQ_3:BPhen acceptor layer: (a) 0% (i.e. pristine AlQ_3 layer), (b) 20%, (c) 50%, and (d) 100% (i.e. pristine Bphen layer).

Another figure of merit of photodetectors is their external quantum efficiency (EQE) which determines the photocurrent level relative to the number of photons (of a certain wavelength) incident per unit area of the device per unit time. Therefore, in case of lateral OPDs, it is important to determine whether or not photons incident on the device outside of the gap area contribute to the produced photocurrent. We compared therefore, in *Figure 4.9*, I_{ph} for the same control device under (a) bottom illumination (exposure through the quartz substrate from the opposite side of the electrodes) and (b) top

illumination (exposure through the gap from the opposite side of the quartz substrate). We observe that I_{ph} under bottom illumination is slightly higher (~17% higher), but comparable, to I_{ph} under top illumination (the curves are plotted on a normal vertical scale to help visualize the difference). This confirms the fact that I_{ph} mostly arises from the photogeneration of carriers in the channel area. However, one might consider the entire organic layers area to conduct EQE estimates in lateral OPDs whenever the light is incident from the opposite side of the electrodes, for both top and bottom contact architectures. The bottom illumination could take advantage of the scattering of light from outside of the channel area and/or the internal reflection of light at the top contacts that may lead to an improvement of the absorption.

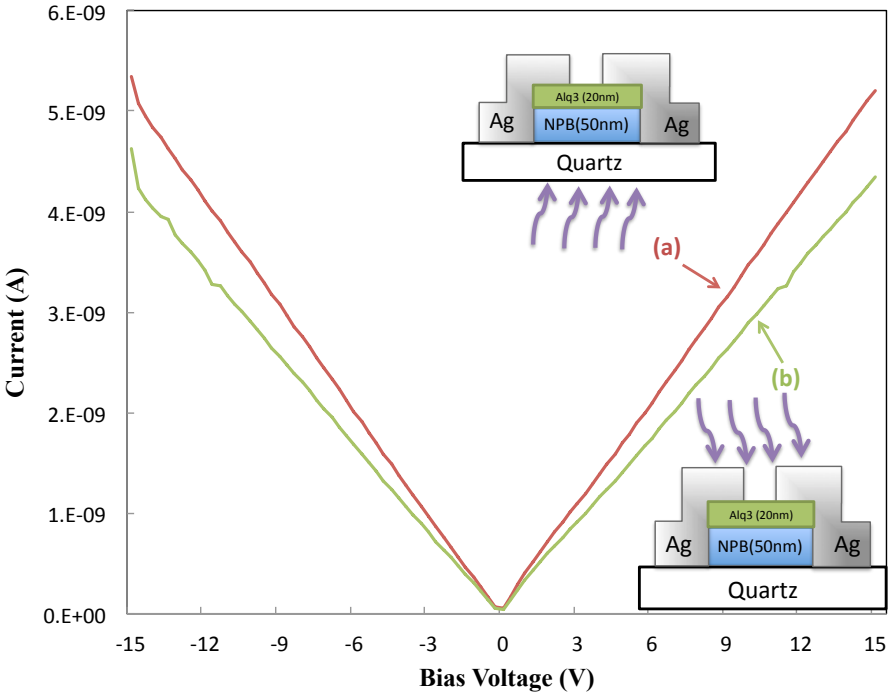

Figure 4.9: Comparison of Iph under (a) bottom illumination and (b) top illumination at a wavelength of 350nm and power density of 0.8mW/cm2.

We also investigated the effect of changing the width of the exposed area of the device on I_{ph}, using for this purpose black tape masks of various widths x (with x varying

from 0.1 to 1.9cm, the widest being equal to the total width of the organic layers), as shown on *Figure 4.10*. The gap area of the OPD is itself covered by the mask, and therefore photons incident on the gap area do not contribute to the photocurrent. Data from tests conducted without using a mask (i.e. x=0) are also shown for comparison. As it is manifested from the figure, I_{ph} decreases upon increasing the mask width, and that I_{ph} approaches I_d only when the mask covers the entire organic layers, indicating as well that photons falling over the entire width of the organic layers (i.e. 1.9 cms) and not only within the gap area, contribute to the photocurrent. The results in *Figure 4.10* indicate as well that accurate determination of EQE in lateral OPDs requires including photons falling over the entire device area, and not just the gap area, in the calculations. The contribution of photons falling outside the gap area to photocurrent can perhaps be attributed to excitons that are formed throughout the NPB layer as a result of absorption, and get dissociated into free electrons and holes at any point along the NPB/AlQ_3 interface, which may then diffuse towards the gap where the one of the carriers can be swept by the electric field towards the opposite electrode. It is also possible that some of these photons are scattered and internally reflected within the organic layers, and thus may produce excitons in the gap area where collection of free carriers by the bias field is more efficient.

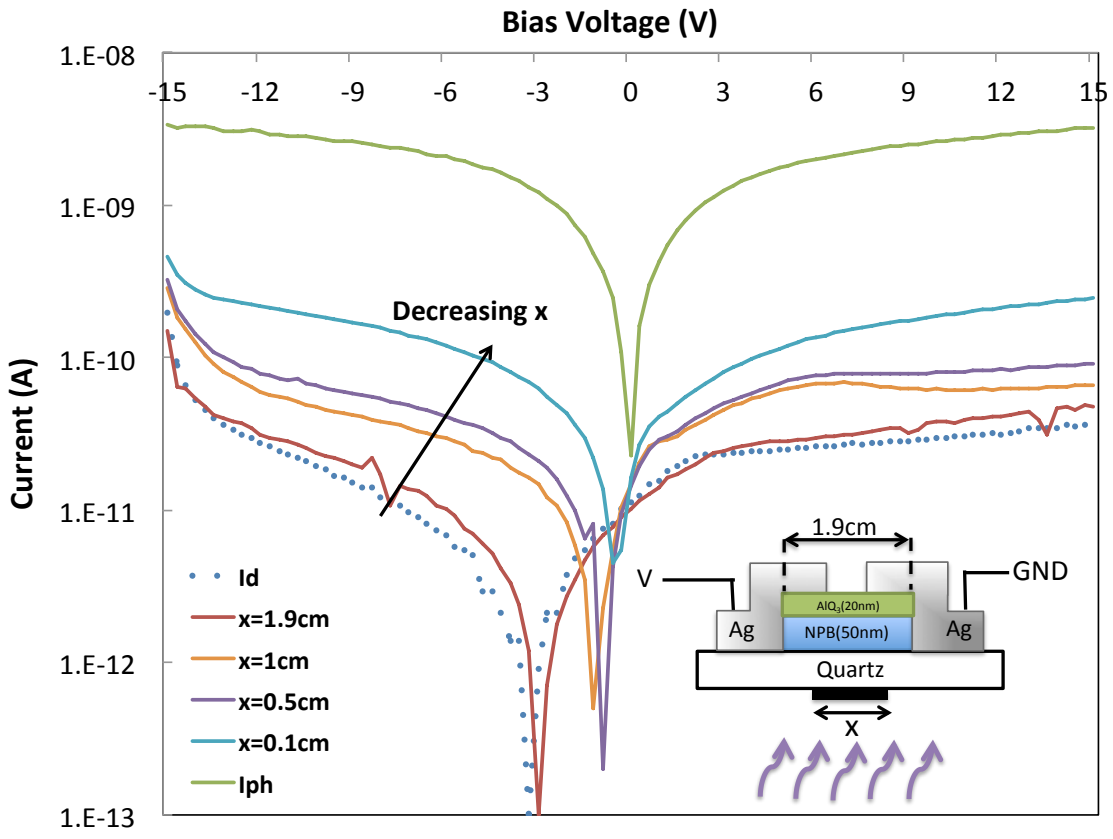

Figure 4.10: Effect of changing the width of the exposed area of the device on I_{ph}, using black tape masks of various widths x (with x varying from 0.1 to 1.9cm, the widest being equal to the total width of the organic layers) covering the channel area.

In conclusion, we find that the dark current of lateral OPDs is strongly limited by space charge limited conduction (SCLC) across a highly depleted gap and arises mostly from transient capacitive currents due to the charge accumulation in the organic layers near the contacts. Similarly, the photocurrent is found to be limited by the collection of photogenerated carriers at the contacts since the donor-acceptor interface is not of prime importance and the use of a high electron mobility acceptor, such as 4,7-diphenyl-1,10-phenanthroline (BPhen), is found to increase the photocurrent. Top and bottom illuminations are also compared and evidence of contribution of light scattering from

outside of the channel area in the case of bottom illumination is reported and should be taken into account when one wants to conduct EQE estimates.

Chapter 5: Study of the cycling stability of the dark and photo currents in lateral OPDs

The reproducibility of the I_d and I_{ph} values for lateral OPDs under repeated light cycles is explored. A lateral OPD being an optical sensor, the stability of its performances is crucial. I_d and I_{ph} should not be altered after the device has been operating in regular conditions in order for the device to maintain a steady detection.

In this work, I-V characteristics of lateral OPDs are obtained in the following manner: after fabrication, an I-V scan is first performed in the dark (i.e. the device being exposed to only an electrical bias). Immediately after, the device is positioned in front of the Hg-Xe lamp and another I-V scan is carried out (i.e. the device being exposed to both electrical bias and illumination). It is therefore important to verify if this simple operation cycle is reproducible for a device with a structure NPB (50nm)/ AlQ_3 (20nm)/ Ag contacts. A first pair of I_d and I_{ph} scans (I_{d1}/I_{ph1}) with the procedure described above is conducted and another cycle is then carried out, giving a second pair (I_{d2}/I_{ph2}), the device being kept in a dry nitrogen atmosphere. Chronologically (1) I_{d1}, (2) I_{ph1}, (3) I_{d2}, and (4) I_{ph2} were measured consecutively and the results are depicted in *Figure 5.1*. As observable in the plot, I_{d2} is significantly higher than I_{d1} while I_{ph1} and I_{ph2} seem totally identical. This variation in I_d compromises the sensitivity since the ratio I_{ph}/I_d decreases after a single operation cycle. Seeing that I_d is strongly affected after the device were exposed to different excitations, the dependences of lateral OPDs performances on the conditions of operation are investigated, i.e. we wanted to investigate how electrical and optical stresses might be affecting both I_d and I_{ph} to produce this behavior.

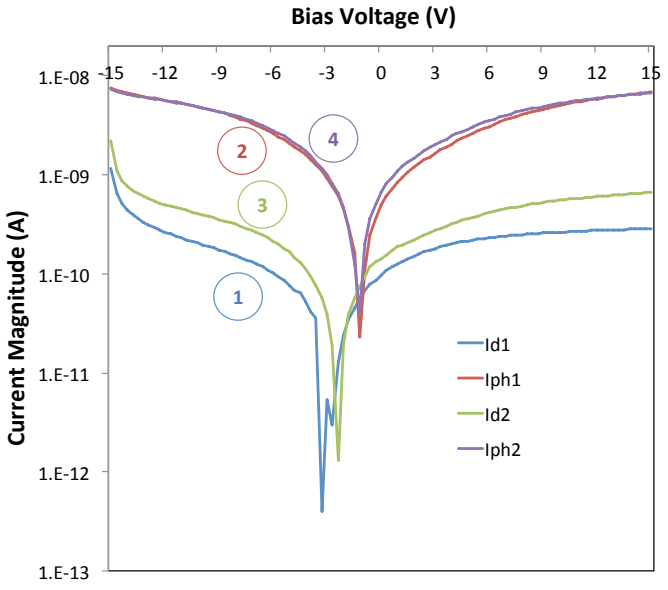

Figure 5.1: Effect of an operation cycle on I_d and I_{ph}.. Chronologically the I_{d1}, I_{ph1}, I_{d2}, and I_{ph2} were measured consecutively.

The reproducibility of I_d while the device is kept in the dark is first studied and the effect of electrical stress only on I_d thus explored. The evolution of I_d immediately after a first I_d scan, the device being kept in the dark is studied on a device with a structure NPB (50nm) / C_{60} (20nm). Two I_d scans, I_{d1} and I_{d2}, from -15V to 15V are thus performed consecutively, as shown in *Figure 5.2,* the device being kept in the dark during the whole process. From the figure it can be observed that I_{d1} and I_{d2} are essentially identical, i.e. the I-V characteristics are completely reproducible in the dark without any influence from electrical stress or previous measurements.

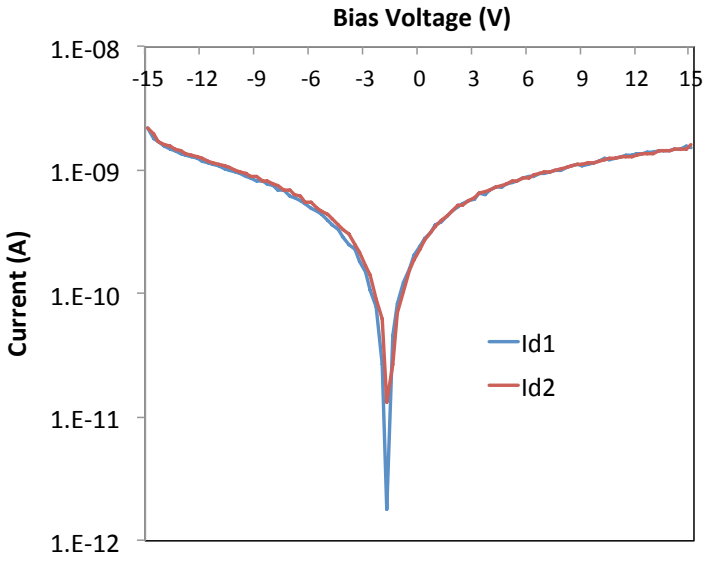

Figure 5.2: Reproducibility of I_d in the dark. I_{d1} and I_{d2} are two I_d scans performed consecutively.

Subsequently, the effect of exposure to light on I_d is investigated. *Figure 5.3* shows three consecutive I_d scans performed on a single device: (0) I_{d0} is measured before exposure to light, thus immediately after the device fabrication; (1) I_{d1} is measured after the device has been exposed to light for 10 minutes at 350nm; finally (2) I_{d2} is measured after the device has in addition endured an I_{ph} scan, i.e. the device has been exposed to both electrical and optical excitations. From the figure, it can be noticed that I_{d1} is significantly increased in comparison to I_{d0}. A prolonged exposure to light indeed leads to a rise of 218% at 7V in I_d compared to its initial value before illumination. On the other hand, I_{d1} and I_{d2} seem essentially identical which could mean that this effect might only be due to exposure to light and not to both electrical and optical excitations. It can also be observed that the drop at the beginning of the scan (from -15V to -12V) is reduced for both I_{d1} and I_{d2}.

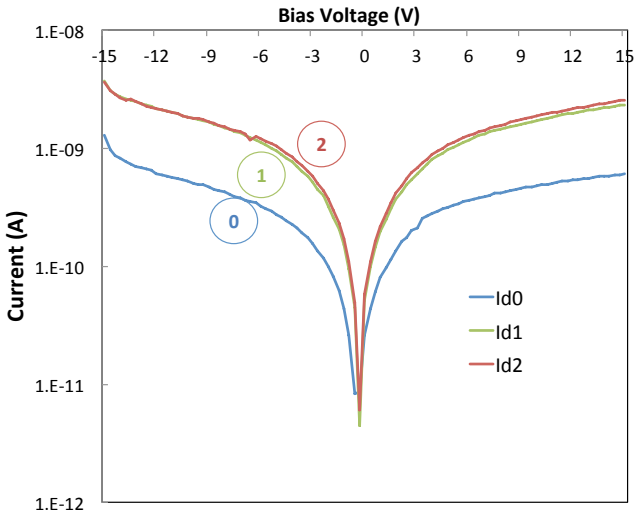

Figure 5.3: Effect of light exposure on I_d. I_{d0} is measured before exposure to light, thus immediately after the device fabrication; I_{d1} is measured after the device has been exposed to light for 10 minutes at 350nm; finally I_{d2} is measured after the device has in addition endured an I_{ph} scan, i.e. the device has been exposed to both electrical and optical excitations.

This increase in I_d might be attributed to an increase in conductivity of the organic layers likely to be due to the filling of charge traps by photogenerated carriers. Charge transport in organic semiconductors being significantly limited by charge trapping, light-assisted trap filling could lead to an enhancement of the conduction thanks to an increase in the concentration of free carriers that contributing to the current flow through the channel.

The increase in I_d could alternatively be due to oxygen-assisted photo-induced doping of the organic layers. Prolonged photo-induced doping has been reported in pentacene based-OTFTs in the presence of oxygen [66]. When organic films are irradiated by light, excitons are created and electron transfer to the oxygen molecule might be possible, forming an organic cation and an O_2^- anion. The cation can transport within the film as a hole, while the O_2^- anion is almost immobile. The combination of both oxygen and light could be therefore critical in lateral ODPs operations. An oxygen-

free fabrication process was adopted by completing all the fabrication in a dry nitrogen atmosphere. After fabrication, the device was encapsulated in order to avoid any exposure to ambient oxygen. Tests on these devices showed I_d was increased of 173% after exposure to light. This proves that this effect is also present in an oxygen-free environment and might be mainly attributed to a trap filling effect as mentioned previously.

Seeing that I_d is highly affected by light exposure, the effect of light exposure on I_{ph} as well as the dependence on the exposure time on both I_d and I_{ph} are studied. *Figure 5.4* shows the evolution with time exposure of both I_d and I_{ph} taken at a bias voltage of 7V of the monolayer device. From the figure, it can be first noticed that after a short exposure to light of only 1minute, I_d is increased by an order of magnitude. A longer exposure leads to a further increase in I_d, but the behavior saturates after an exposure time of 30 minutes. Consequently, it seems that the increase in I_d arises mostly instantaneously after exposure to light and the fact that it is more pronounced after an extended exposure confirms its solely optical origin. Moreover, the fact that the same increase occurs in the case of a monolayer device suggests that the increase in conductivity is due to a bulk effect and not to interfacial traps filling. I_{ph}, in contrast, does not seem to be affected by light exposure and remains steady under prolonged illumination. This is a critical phenomenon that affects lateral OPDs sensitivity since I_d almost reaches the value of I_{ph}.

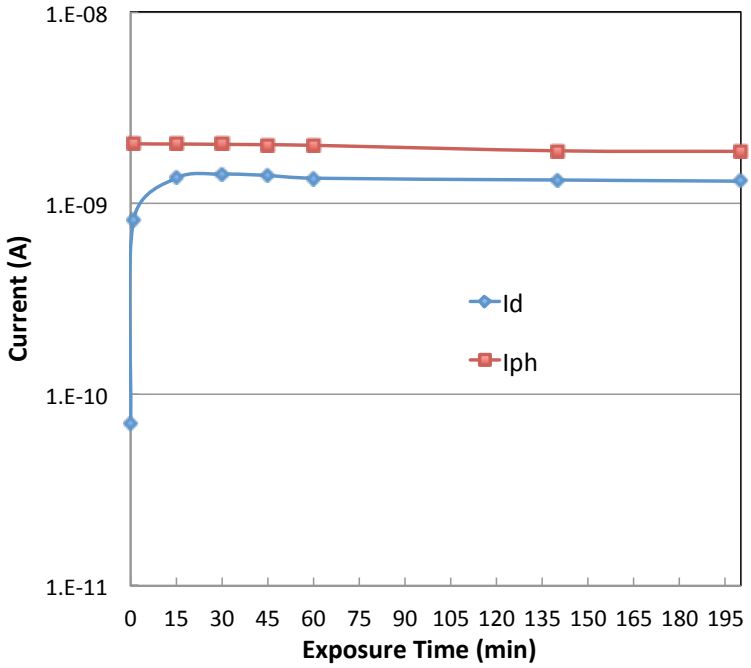

Figure 5.4: Effect of light exposure time on both I_d and I_{ph} values taken at a bias voltage of 7V.

This behavior is described as a being a "memory effect", i.e. I_d increases after exposure to light and tends to behave similarly than I_{ph}. It is noticeable that I_d after light exposure gains in symmetricity and the drop usually seen at the beginning of a scan decreases. This suggests that the SCLC effect that dominates I_d is less predominant after exposure to light and that the leakage current through the channel is enhanced. It is verified when we investigate the effect of the scan rate on I_d after prolonged exposure to light for a monolayer device. In a previous chapter, it has been shown that increasing the sweep rate (i.e. decreasing the sweep time) led to a significant increase in I_d, which was consistent with a lower density of space charges that limits I_d. However, I_{ph} were not significantly affected by the change in the sweep rate. *Figure 5.5* shows the dependence on the scan duration of I_d taken after the device was exposed to light for 30 minutes. It can be seen that I_d after exposure is no longer affected by the scan rate since longer scans

do not lead to a decrease in I_d as seen before and I_d tends therefore to behave like I_{ph} with a predominant conduction through the channel.

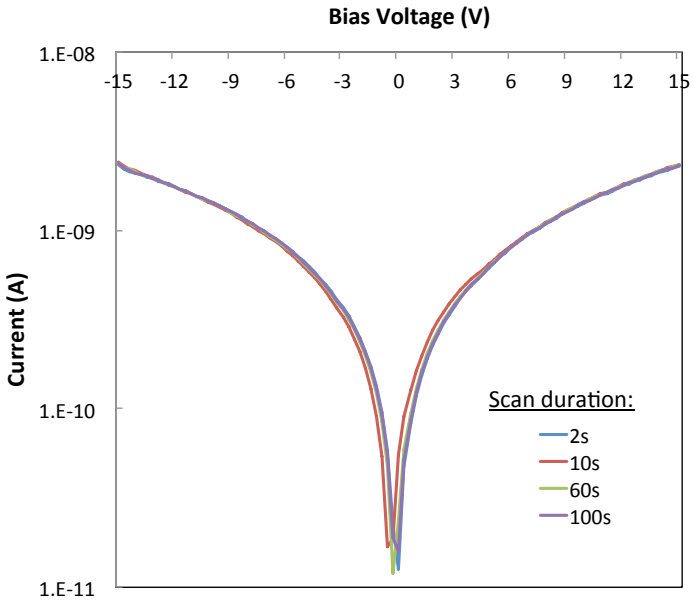

Figure 5.5: Dependence on the scan duration of I_d taken after the device was exposed to light for 30 minutes.

The encountered memory effect is attributed to trap filling which makes the organic layers, and therefore the channel more conductive and it is likely that the leakage current through the channel increases after illumination. *Figure 5.6* shows indeed that the device exposed to a top-illumination for 1 minute, i.e. the light irradiating only the channel, exhibits an analogous increase in I_d. The evolution of the asymmetricity is also noticeable.

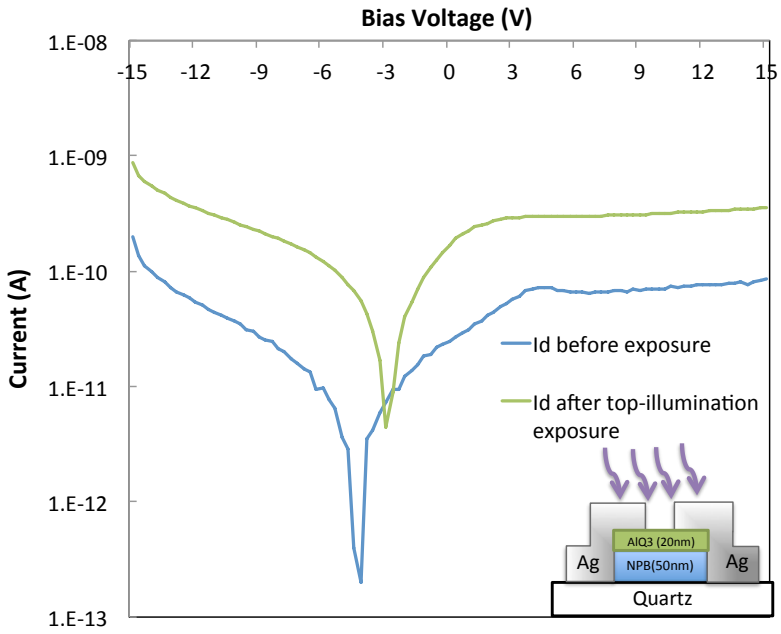

Figure 5.6: Increase of I_d after top-illumination exposure (only the channel is exposed to light).

The durability of this memory effect on I_d is next explored and presented in *Figure 5.7* The device is again exposed to light for 10 minutes and the evolution of I_d with time is recorded. The device is kept in dry nitrogen atmosphere to avoid any ambient degradation. The I_d values are taken at a bias voltage of 7V and are normalized to the value of I_{d0} before exposure to light. Similarly to what has been depicted above, the exposure to light leads to an increase in I_d (ratio of ~3.4 with I_{d0}). Nevertheless, it can be seen that this memory effect is not permanent since the value of I_d after 180 minutes of exposure time is almost attaining the initial value of I_{d0} before exposure. Moreover, a re-exposure to the same light for only 1 minute results in a comparable increase in I_d making this memory effect reversible and recoverable.

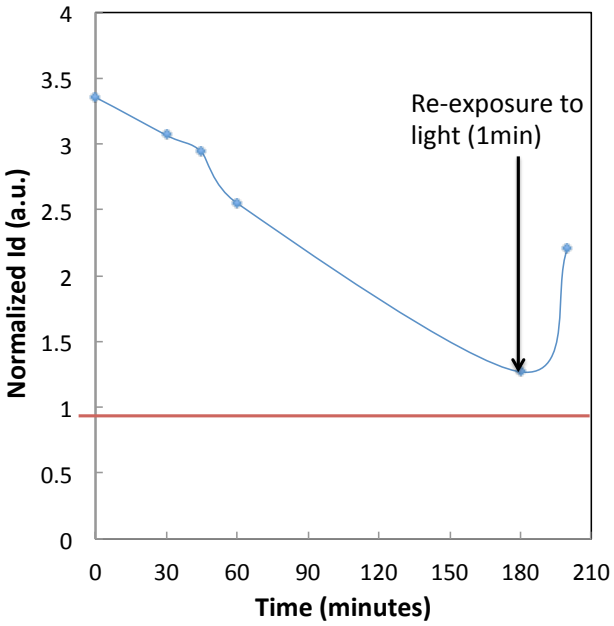

Figure 5.7: Durability of the memory effect and recovery after re-exposure to light. The values of I_d are normalized to the I_d value before exposure to light.

These traps remain filled by carriers for a long period of time and these trapped carriers are hardly de-trapped by the application of an external electric field. A lateral OPD was exposed to light for 30 minutes and 11 repeated I_d scans were then performed, from I_{d0} to I_{d10}, i.e. I_{d0} (instantaneously after exposure to light) is immediately followed by another I_d scan, I_{d1}, and I_{d1} immediately followed by I_{d2} etc. *Figure 5.8* shows I_d after exposure to light (I_{d0}) and I_d after the 11^{th} scan (I_{d10}). It can be seen that I_{d0} and I_{d10} are identical confirming the fact that the traps remain filled even with application of an external field. Increasing the voltage range did not affect I_d either. It is likely to be due to the low electric field across the wide channel that might not allow the carriers to be removed from deep traps.

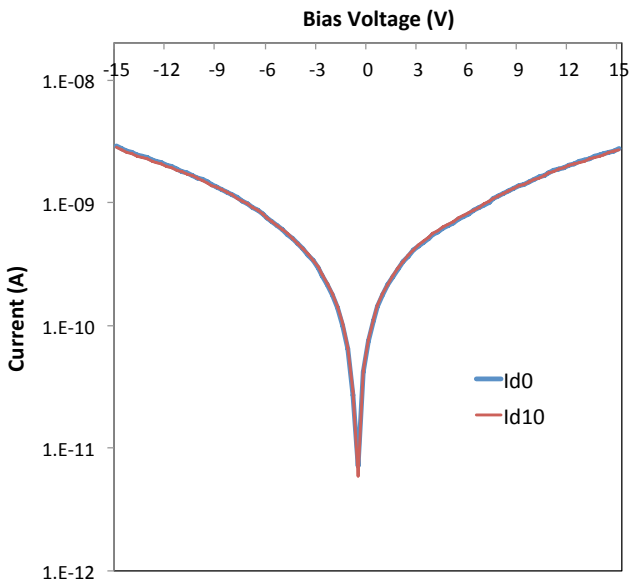

Figure 5.8: Permanency of the memory effect with repeated exposure to external electric field. I_{d0} is taken immediately after light exposure and I_{d10} is taken after 11 consecutive scans.

These findings suggest that the detectivity of lateral OPDs is strongly influenced by exposure to light since only I_d is increased while I_{ph} remains constant, leading to a decrease in the ratio I_{ph}/I_d after exposure. However, in a more general perspective, these results imply that organic films conductivity can be intrinsically increased by trap filling thanks to exposure to light in the absence of oxygen, phenomenon that still has not been reported in vertical OPDs and OSCs. The lateral architecture helps to visualize this effect since its I-V characteristics are mostly limited by the poor mobility of the organic layers due to the wide lateral dimensions (a few micrometers) whereas vertical devices, with a typical thickness of a 100 nanometers, are primary limited by exciton dissociation and carrier extraction.

These preliminary results offer some new perspectives of work to fully describe this effect. Indeed, it is important to depict the nature (interfacial, surface, or bulk states) of the traps that are being filled by light exposure. The spectral dependence of this effect

with the determination of the onset wavelength of its occurrence as well as its evolution with temperature could also lead to noteworthy conclusions on the energy of the filled traps.

Chapter 6: Lateral OPDs for deep ultraviolet applications

OPDs are promising for deep ultraviolet detection (DUV) detection, i.e. for detection of wavelengths below ~320nm, since organic semiconductors show wide optical band gaps (1.5-3.0 eV). Recently, a few vertical OPDs operating in the DUV band have been reported [67-69]. However, a vertical architecture requires illumination through a transparent electrode or transparent substrate/electrode combination; a requirement that is often hard to realize at these wavelengths. The limitation of the use of the common ITO/glass substrates that strongly absorb wavelengths shorter than 350nm has been mentioned in a previous chapter.

Some alternatives have been employed to overcome this issue. Conducting polymer poly(3,4-ethylenedioxythiophene)-poly(styrenesulfonate) (PED-OT:PSS) with high transmittance in the DUV region has been used as transparent anode on quartz substrates [67, 68] for OPDs performing under bottom illumination. OPDs working under top illumination using classic ITO anodes have also been reported employing an ultra-thin Al cathode (12nm) [69]. It is proposed in this work to use lateral OPDs under bottom illumination for DUV detection, as the use of a transparent electrode is not required. Moreover, lateral OPDs could be potentially advantageous stability-wise since PED-OT:PSS anodes are deposited by solution processes and their use could lead, in the long term, to diffusion of moisture in the organic active layers. DUV OPDs employing an ultra-thin cathode are also likely to undergo strong ambient degradation due to a fragile top capping.

A certain number of D-A systems have been used for vertical DUV OPDs. The good detection in the DUV region of these devices were mainly attributed to the presence of a strong absorption peak between 250nm and 300nm of some acceptor materials, such as BAlQ and BPhen [67, 69]. Detectivities of ~10^{12} Jones, comparable to inorganic Si photodetectors, were reported by *Zhu et al. (2011)* [67] at 270nm and by *Wu et al. (2010)* [68] at 280 using NPB:BAlQ(ratio 1:1, 80nm) and m-MTDATA(10nm) / m-MTDATA:BPhen (1:1, 60nm)/ BPhen (10), respectively, as active area structures. The absorption spectra from 200nm to 450nm of these 4 materials are depicted in *Figure 6.1* for 30nm-thick films. In this chapter, the performances of DUV lateral OPDs using similar D-A systems are investigated and compared to vertical OPDs ones.

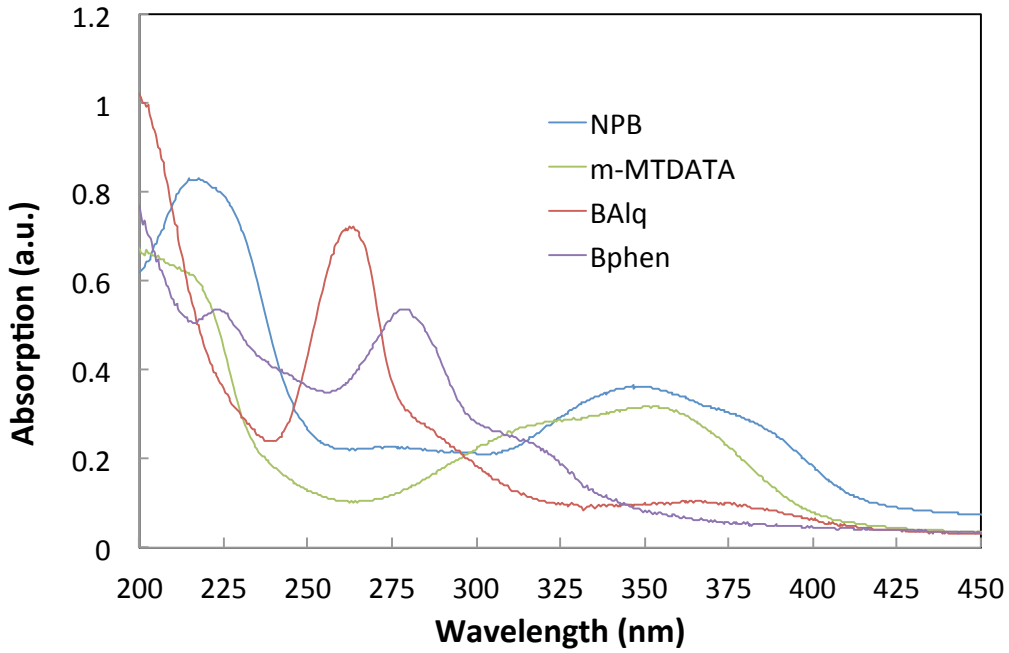

Figure 6.1: Absorption from 200nm to 450nm of NPB, BAlQ, m-MTDATA, and BPhen.

First is studied the D-A system made of NPB as donor material and BAlQ as acceptor material. Three different structures were investigated: (a) NPB (50nm) / BAlQ (20nm) / contacts; (b) BAlQ (50nm) / NPB (20nm) / contacts; and (c) NPB : BAlQ (1:1,

70nm) / contacts. External Quantum Efficiency (EQE) estimates, which determine the photocurrent level relative to the number of photons (of a certain wavelength) incident per unit area of the device per unit time were manually calculated using the following formula $EQE = \frac{E_\lambda . I_{ph}}{J_L . A}$ where E_λ is the energy of a photon at the wavelength λ in eV; I_{ph} is the photocurrent in A; J_L is the light power density at the wavelength λ in W/cm^2; and A is the active area in cm^2. Since, as mentioned in a previous chapter, most of the photoresponse arises from the gap area, we assumed that *A* was limited to the gap area, i.e. $A = 25\mu m$ x 4mm = 0.001cm^2.

EQE estimates at 4 different wavelengths (270nm, 300nm, 350nm, and 400nm) taken at a bias voltage of 7V for device (a), (b), and (c) are given in *Figure 6.2*. The inset displays the absorption spectra of NPB and BAlQ. First, it can be observed that lateral OPDs exhibit in general low efficiencies ($< 10\%$) in accordance with reported studies. For example, *Ho et al.* reported bilayer bottom-contact lateral OPDs with an EQE reaching 12% at 552nm at very high applied field (12.5V/μm) [52]. The devices reported in this work operate a lower voltages and reach an EQE of $\sim$8.3% at 270nm which is the highest EQE value reported for lateral OPDs operating in the UV-DUV range.

However lateral OPDs hardly compete with vertical architectures in terms of efficiency. For example, *Zhu et al*. reported a vertical OPD comprising the same donor-acceptor system with an EQE of 63% at 270nm at -12V[67] .The low efficiencies of lateral OPDs are mostly due to the low photocurrents (10^{-9}-10^{-8} A) largely limited by the collection of the free carriers as mentioned in a previous chapter. The very poor EQE values ($\sim$1%) at each wavelength for device (c) made of a single BHJ active layer also

suggest that the transport of photogenerated carriers is more critical to I_{ph} in comparison to light absorption or exciton dissociation. Devices (a) and (b) however demonstrate changes in efficiencies with respect to the wavelength of illumination. Both devices show their highest and lowest efficiencies at 270nm and 400nm, respectively, which is mostly explained in terms of absorption strength. Both NPB and BAlQ are poorly absorbing at 400nm lowering hence the limited photogeneration of free carriers at this wavelength. The fact that device (b) shows higher efficiency at 270nm in comparison to device (a) is mostly attributed to the stronger absorption in the bottom BAlQ layer compared to the NPB absorbing layer. Knowing that I_{ph} is also strongly collection limited, the bipolar nature of NPB with both high electron and hole mobilities [67] might also contribute to an enhanced collection through the top NPB layer in device (b). This faster collection might also explain the slightly higher efficiency of device (b) at 300nm (wavelength at which the absorption intensities of BAlQ and NPB are similar) as well as the small difference in EQEs between devices (a) and (b) at 350nm (wavelength at which NPB is significantly more absorbent than BAlQ).

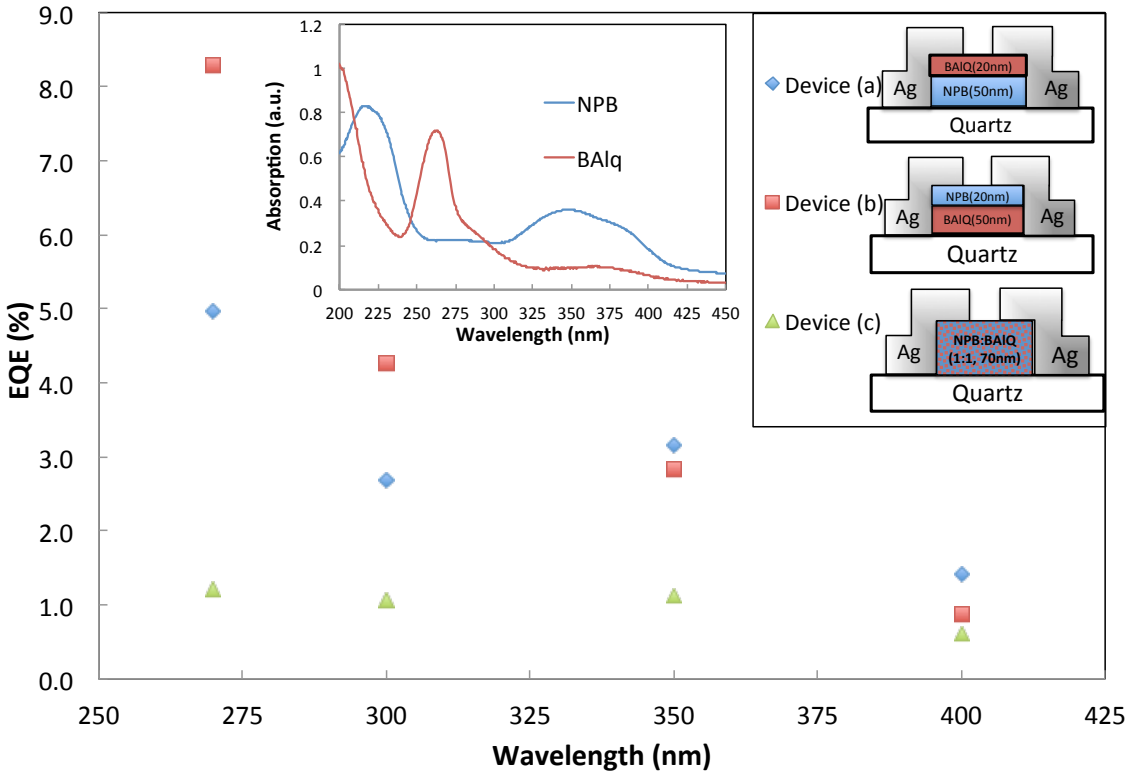

Figure 6.2: EQE values taken at a bias voltage of 7V and 4 different wavelengths (270nm, 300nm, 350nm, and 400nm) for 3 device structures: (a) NPB (50nm) / BAlQ (20nm) / contacts; (b) BAlQ (50nm) / NPB (20nm) / contacts; and (c) NPB : BAlQ (1:1, 70nm) / contacts. The inset displays the absorption spectra of NPB and BAlQ

We then explored a different D-A system made of m-MTDATA as donor material and BPhen as acceptor material. The same three structures are characterized: (a) m-MTDATA (50nm) / BPhen (20nm) / contacts; (b) BPhen (50nm) / m-MTDATA (20nm) / contacts; and (c) m-MTDATA : BPhen (1:1, 70nm). The EQE estimates are shown in *Figure 6.3* (compared to the previous set of devices the shortest wavelength is now 280 and not 270 in order to benchmark with literature results) and the absorption spectra of m-MTDATA and BPhen are presented in inset. A similar trend is observable for this set of devices.

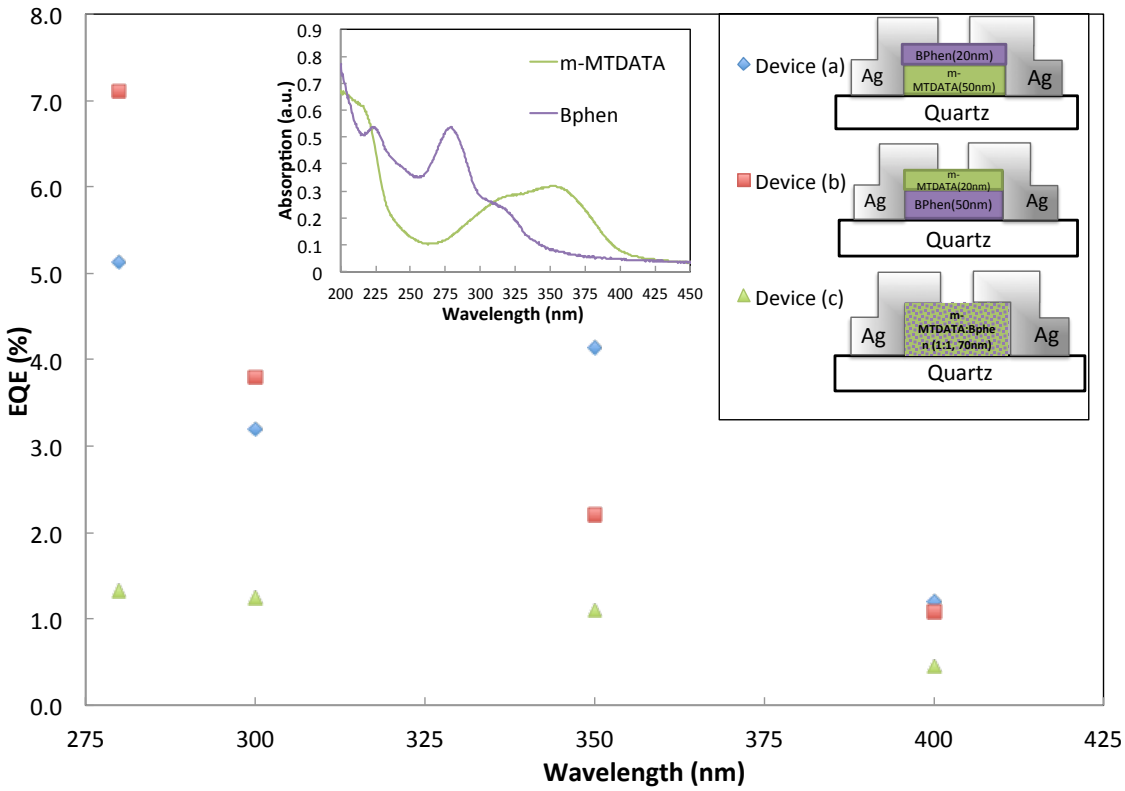

Figure 6.3: EQE values taken at a bias voltage of 7V and 4 different wavelengths (280nm, 300nm, 350nm, and 400nm) for 3 device structures: (a) m-MTDATA (50nm) / BPhen (20nm) / contacts; (b) BPhen (50nm) / m-MTDATA (20nm) / contacts; and (c) mpMTDAT : BPhen (1:1, 70nm) / contacts. The inset displays the absorption spectra of m-MTDATA and BPhen.

Figure 6.4 compares the EQE values of a device structure type device (a) for the two different D-A systems. The inset is the absorption spectra of the 4 organic materials used. It can be seen from the figure that the two systems exhibit similar efficiencies. From an absorption stand point, one could expect the combination NPB-BAlQ to show higher efficiencies at 270nm-280nm, 300nm, and 350nm. However, the chart shows that the device based on m-MTDATA and Bphen have higher efficiencies at these wavelengths, which is mostly attributed to the higher mobility of Bphen compared to BAlQ improving thus the collection through the top layer.

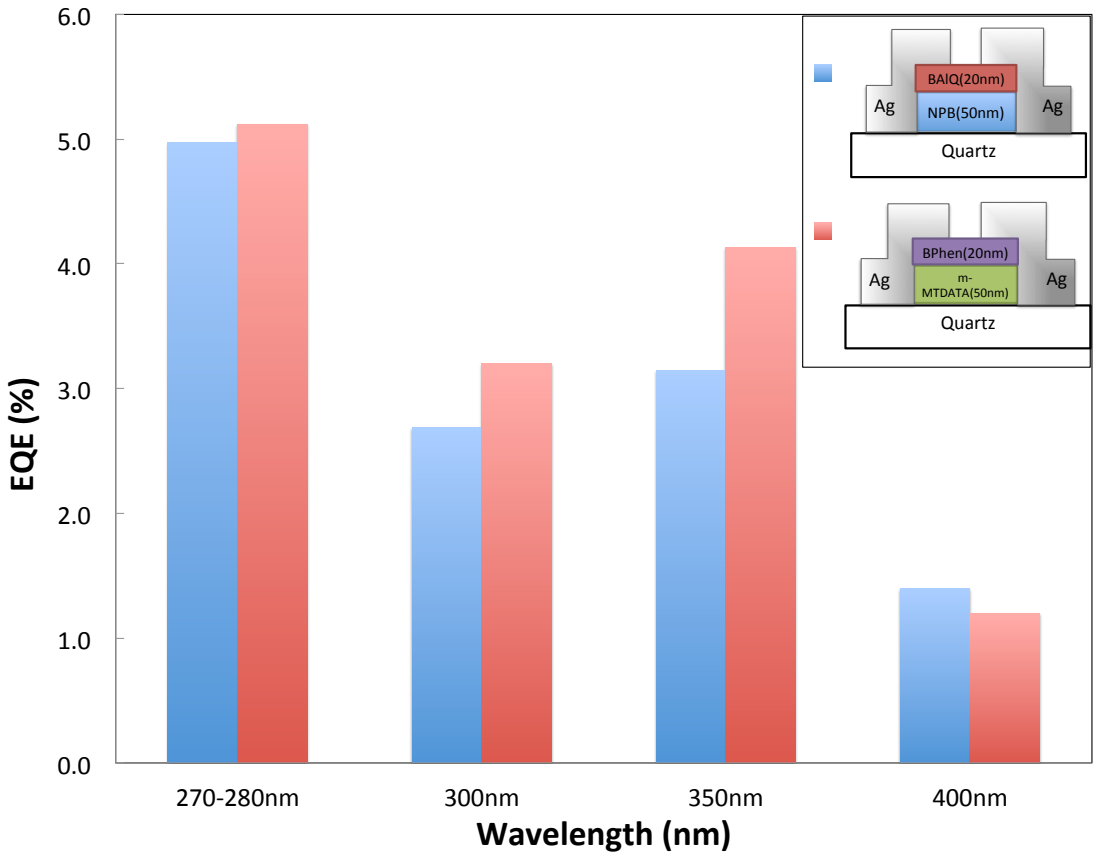

Figure 6.4: Comparison of performances between the two donor-acceptor systems in the case of a device structure type (a).

Figure 6.5 shows similar data than *Figure 6.4* but for devices with a structure type (b). Analogously, the device with a top layer made of NPB exhibits in general a higher efficiency in general than the one using m-MTDATA. This could be again attributed to the higher carrier mobility (around two orders of magnitude higher) in NPB films compared to m-MTDATA one [70].

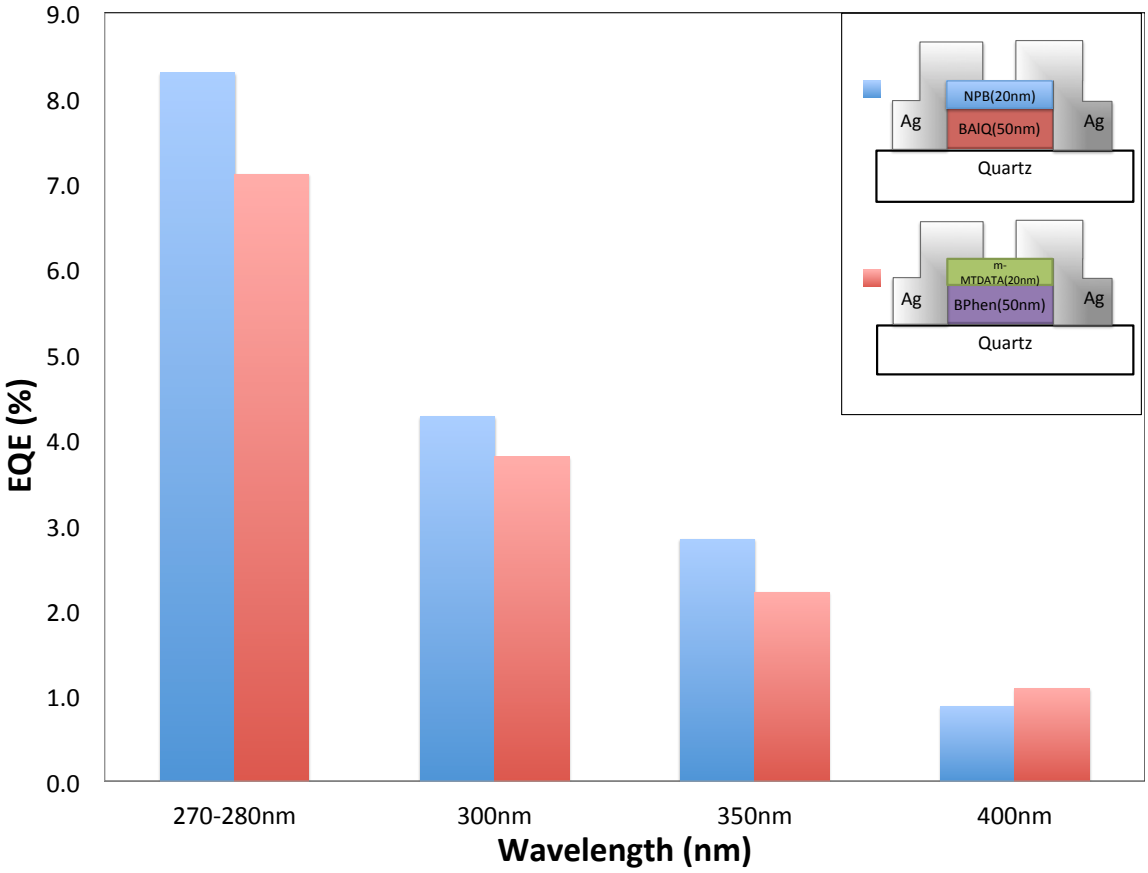

Figure 6.5: Comparison of performances between the two donor-acceptor systems in the case of a device structure type (b).

For comparison purposes with reported vertical DUV OPDs using the same D-A systems and already mentioned above, some detectivity (D^*) estimates are given for lateral OPDs in the DUV range. D* values at a bias voltage of 7V are evaluated for device structures type (b) for both D-A systems since they exhibit the highest efficiencies at the shortest wavelengths. Structures BAlQ (50nm) / NPB (20nm) and BPhen (50nm) / m-MTDATA (20nm) show D^* of 4.22 10^{10} Jones at 270nm and 3.91 10^{10} Jones at 280, respectively. Consequently, the detectivity of lateral OPDs is significantly lower than vertical ones due I_{ph} being strongly limited by carrier collection.

From the above findings, it can be concluded that organic semiconductors are suitable for DUV applications due to their high absorption for wavelengths shorter than 320nm. However, lateral architectures, whose efficiencies are strongly limited by carrier collection, hardly compete again vertical ones in terms of efficiency and detectivity.

Chapter 7: Phosphorescent sensitized bottom absorbing layer in lateral OPDs

The EQE of an OPD is proportional to the absorption efficiency of the device, which is defined as the ratio of the number of excitons created to the number of absorbed photons. The Beer-Lambert law states that the absorption is enhanced when the length of absorption, i.e. the thickness of the absorbing layer, is increased. In organic materials, there is however a tradeoff between absorption and exciton recombination rate when increasing the thicknesses. Indeed, a too thick absorbing layer would compromise the collection efficiency of the device due to a poor charge transport, which would lead to a decrease in the overall EQE. Optimized thicknesses for absorption and collection in lateral OPDs have been discussed in a previous chapter of this thesis.

The recombination rate is directly related to the exciton diffusion length L_D which depends on the exciton lifetime. In other words, extending the exciton lifetime would allow excitons to travel longer distances before they recombine (or dissociate) and therefore would potentially enable to deposit thicker absorbing layers. As described previously, the absorption of a photon in organic materials is governed by a selection rule and leads thus in general to the creation of a singlet excited state (spin allowed transition). Singlet states exhibit however short lifetimes ($\sim$ns) and undergo very fast decay. In contrast, triplet states decay is longer (lifetime $\sim\mu s$) since such a transition is spin forbidden in fluorescent materials. Therefore, introducing long lifetime, and thus long diffusion length triplet states in

the bottom absorbing layer made of fluorescent materials would potentially enable to improve the absorption and the overall efficiency of lateral OPDs.

In this work, a phosphorescent sensitizer is introduced into the bottom absorbing layer. Phosphorescent molecules incorporate heavy atoms that allow a strong spin-orbit coupling. Therefore phosphorescent molecules demonstrate in general rapid Intersystem Crossing (ISC), which corresponds to a radiationless transition between isoenergetic levels of different spin multiplicity, i.e. effective transitions from singlet excited states to triplet states become possible. Doping a fluorescent-host matrix with a complementary phosphorescent guest could lead to an intramolecular energy-transfer scheme, as drawn in *Figure 7.1*. The absorption of a photon by a fluorescent host molecule creates a singlet exciton S_1(Fl. host). If the phosphorescent guest molecule band gap is smaller than the one of the host, a long-range Forster energy transfer from S_1(Fl. host) to S_1(Ph. guest) can occur very effectively, even at low doping concentrations. S_1(Ph. guest) can then rapidly undergo ISC, forming a triplet exciton T_1(Ph. guest) that can triplet energy transfer back to the host if T_1(Fl. host) is energetically favorable. Such an energy transfer pathway would potentially enable to create long-lived triplet excited states.

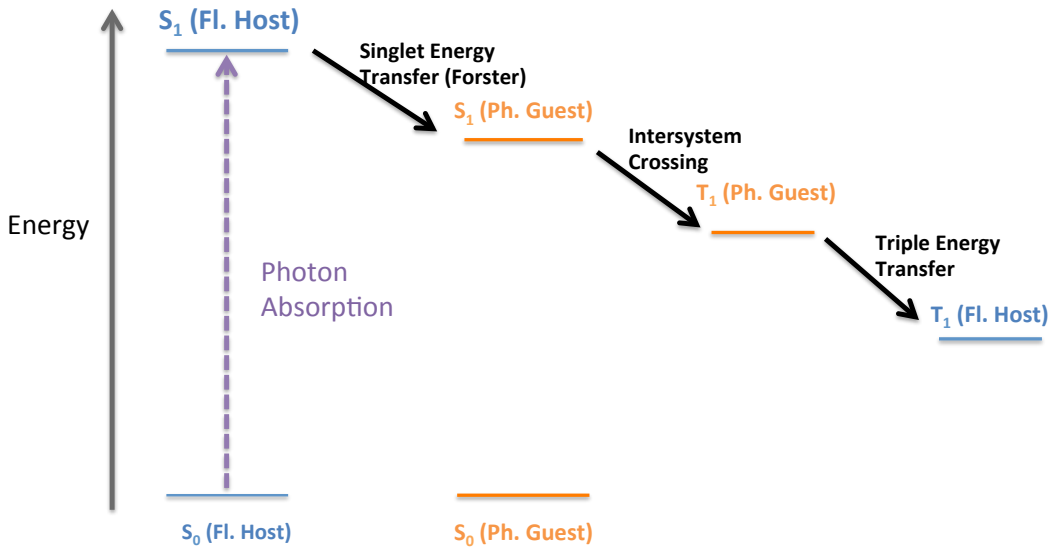

Figure 7.1: Energy-transfer scheme of a phosphorescent-sensitized absorbing layer.

Two complementary host-guest systems have been identified in this work. In both of them, NPB is used as fluorescent host and two phosphorescent guests, bis[2-(4,6-difluorophenyl)pyridinato-C^2,*N*](picolinato)iridium(III) (FIrpic) and tris(2-phenylpyridine)iridium ($Ir(ppy)_3$) are tested. The HOMO-LUMO levels and first triplet T_1 state energy are indicated in *Table 7.1.*

Material	LUMO (eV)	HOMO (eV)	T_1 (eV)
NPB	2.4	5.4	2.3
FIrpic	3.2	5.8	2.6
$Ir(ppy)_3$	2.9	5.2	2.6

Table 7.1: HOMO-LUMO levels and first triplet state energy of NPB, FIrpic, and $Ir(ppy)_3$.

The use of these two systems is also justified by photoluminescence (PL) spectroscopy. *Figure 7.2* shows the PL spectra of (a) NPB:FIrpic and (b) NPB:$Ir(ppy)_3$ blends for different phosphorescent guest concentrations (0%, 2%, 5%, 8%, and 10%). It can be noticed that in both mixture the PL due to the emission

of NPB at ~465nm is severely quenched when a phosphorescent guest is introduced, even at very low concentrations. This confirms that the energy-transfer scheme developed above, i.e. the guest-assisted transfer of NPB singlet excitons to NPB triplet excitons that are not "allowed" to decay, is actually effective in both systems. In the rest of the chapter, NPB (95%):FIrpic (5%) blends are investigated instead of NPB:$Ir(ppy)_3$ mixtures for two main reasons: (i) it can be observed in NPB:$Ir(ppy)_3$ blends PL spectra a small peak at ~520nm corresponding to $Ir(ppy)_3$ green emission and thus representative of an incomplete back energy transfer of triplet guest excitons to the host (less energy-favorable); (ii) the HOMO of FIrpic (5.8eV) is deeper than the one of NPB (5.4eV) in contrast to $Ir(ppy)_3$ (5.2eV) which reduces hole trapping in the doped layer.

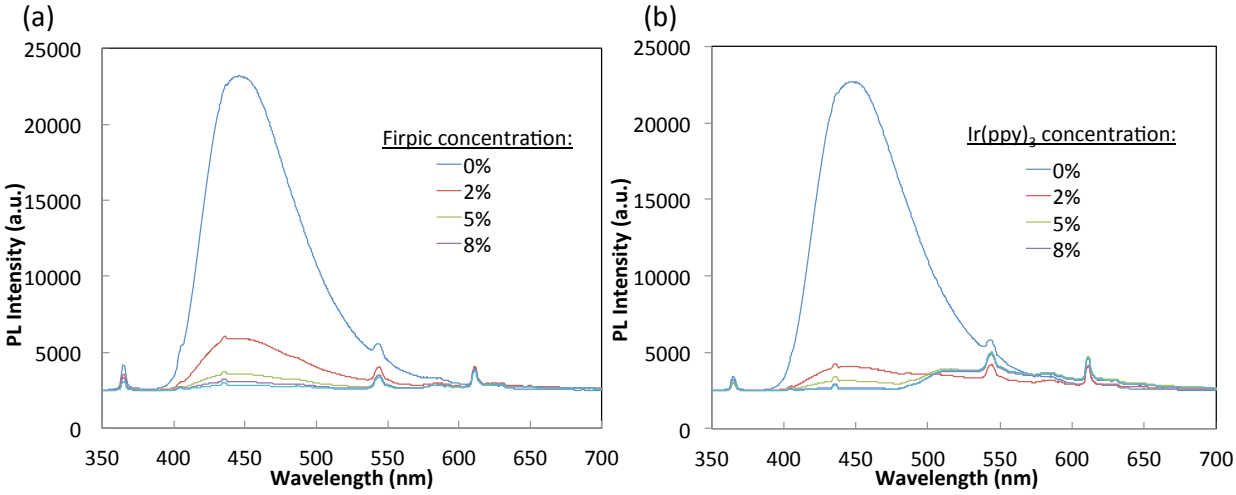

Figure 7.2: PL spectra of (a) NPB:FIrpic and (b) NPB:$Ir(ppy)_3$ blends at different dopant concentrations.

To achieve efficient photogeneration of free carriers via this process, it is important to find an acceptor material with a deep LUMO capable of dissociating the very stable NPB triplet excitons (T_1(NPB) ~2.3eV). Three acceptors materials (BAlQ, TPBi, and C_{60}) have been tried on lateral OPDs with a structure NPB (95%):FIrpic

(5%) (50nm) / acceptor (20nm). *Figure 7.3* shows I_{ph} values (taken at a bias voltage of 7 V) of the three different structures normalized to the corresponding I_{ph} value of devices with a conventional structure NPB (50nm) / acceptor (20nm). The different energy levels are also included in the figure. As can be seen on the figure, the devices comprising a phosphorescent-sensitized absorbing layer exhibit unexpectedly lower I_{ph} values in comparison to the corresponding un-doped devices for the three tested acceptor materials. The creation of long diffusion length NPB triplet excitons does not seem to improve the photoresponse of these devices. Knowing that lateral OPDs efficiency is strongly collection limited, the loss in photoresponse might be attributed to an increased charge trapping in the doped absorbing layer due to the presence of guest impurities. This charge trapping might have a critical impact, especially near the donor-acceptor interface, since most of the collection is likely to occur in the top acceptor layer.

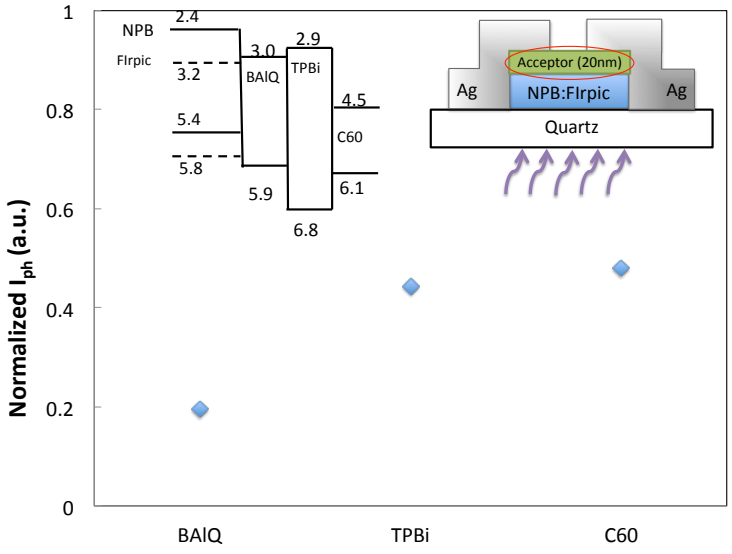

Figure 7.3: I_{ph} values (taken at a bias voltage of 7 V) of lateral OPDs with a structure NPB (95%):FIrpic (5%) (50nm) / acceptor (20nm) normalized to the corresponding I_{ph} value of devices with a conventional structure NPB (50nm) / acceptor (20nm). BAlQ, TPBi, and C_{60} are tested as acceptor materials.

To investigate the effect of the charge trapping effect near the donor-acceptor interface, devices with structures NPB (95%):FIrpic (5%) (50nm) / NPB (x nm) / C_{60} (20nm) are tested for x = 0, 10, 20 and 40nm. The I_{ph} values are taken at bias voltage of 7V and normalized to the corresponding I_{ph} value of the standard device NPB (50nm) / C_{60} (20nm) and are displayed in *Figure 7.4.* It can be noticed that incorporating a neat NPB layer, with a thickness up to 20nm, between the doped absorbing layer and the top acceptor layer improves significantly the photoresponse of phosphorescent-sensitized devices (improvement of around 50%). This could be attributed to a decrease of the charge trapping near the interface. However, their performances still remain lower than a standard device and might be limited by other factors. A further increase of this interfacial layer thickness leads nevertheless to a decrease in I_{ph}, which might be attributed to an increase of NPB triplet excitons recombination before they reach the donor-acceptor interface.

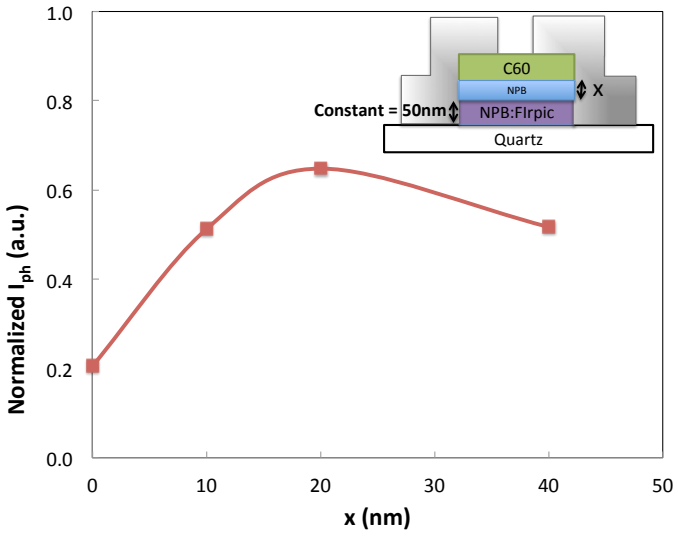

Figure 7.4: I_{ph} values are taken at bias voltage of 7V of lateral OPDs with a structure NPB (95%):FIrpic (5%) (50nm) / NPB (x nm) / C_{60} (20nm) with x = 0, 10, 20 and 40nm. The I_{ph} values normalized to the corresponding I_{ph} value of the standard device NPB (50nm) / C_{60} (20nm).

It is possible that the charge trapping in the bulk of the doped absorbing layer remain significant and limits the collection. The loss in photoresponse might also be due to a decrease in the exciton dissociation efficiency. NPB triplet excitons are very stable and their dissociation (sensitized and/or field-induced) might be harder than in the case of singlet excitons. Furthermore, triplet excitons migrate and diffuse to a dissociative site via triplet energy transfer. Singlet excitons diffuse via a long-ranged Forster mechanism, triplet excited states often diffuse via Dexter energy transfer, which has an exponential distance scaling [71]. This can result in lower diffusivities for triplet excitons compared to singlets, potentially negating enhancements in L_D that result from the increased triplet exciton lifetime.

Chapter 8: Conclusions and Future Work

8.1. Conclusions

To summarize, top-contact lateral OPDs were fabricated and characterized. A thermal evaporation-only fabrication process was used, in which a thin wire is used as a shadow mask to create a gap between the two co-planar electrodes.

A device made of a bilayer heterojunction, using NPB as donor and AlQ_3 as acceptor materials, is found to exhibit a good photo-response, reflected in a substantially higher current flow under illumination versus that in the dark (around 100 times higher). It was noticed however that the dark and photo-currents show different dependences on the applied voltage suggesting they may be governed by distinct phenomena.

It was found that starting I-V scans at a non-zero bias, e.g. $\pm$15V, instead of 0V leads to highly asymmetric I_d trends, causing the minimum-current point to occur at a negative or a positive voltage instead of zero. Moreover a fast decrease in I_d was noticed in the beginning of the scan when started at high voltages suggesting the rapid formation of space charges in the organic layers, most likely near the edges of the metallic contacts as soon as carriers are first injected into it. The rapid formation of space charges can be attributed to the very poor conduction across the gap due to the low carrier mobility of organic semiconductors. This perhaps explains the remarkably low dark current levels in lateral OPDs over a relatively wide bias range. It was finally concluded that, except at very low bias levels ($<\pm$~2V) where current is limited by injection from the contacts, the dark current in lateral OPDs is primarily limited by space charge limited conduction (SCLC) across a highly depleted (i.e. essentially insulating) gap, and is dominated by

capacitive transients. The component of I_d arising from the steady-state drift of carriers across the gap is much smaller in comparison, and is perhaps significant only at high bias voltages.

The photocurrent characteristics, on the other hand, remain essentially symmetric regardless of the scan direction which therefore suggests the formation of a conductive "channel" for charge transport across the gap only when under illumination. The formation of this channel across the otherwise depleted gap becomes possible due to the much higher carrier concentration as a result of photogeneration. However, the photocurrent is found to be limited by the collection of photogenerated carriers at the contacts since the donor-acceptor interface is not of prime importance and the use of a high electron mobility acceptor, such as BPhen, was found to increase the photocurrent.

Another figure of merit of photodetectors is their external quantum efficiency (EQE) which determines the photocurrent level relative to the number of photons (of a certain wavelength) incident per unit area of the device per unit time. Therefore, in case of lateral OPDs, it was important to determine whether or not photons incident on the device outside of the gap area contribute to the produced photocurrent. Top and bottom illuminations were thus compared and evidence of contribution of light scattering from outside of the channel area in the case of bottom illumination was reported and should be taken into account when one wants to conduct EQE estimates.

The stability of the dark and photo-currents over multiple operation cycles was also investigated. It was found that the dark current significantly increases after the device is exposed to light while the photocurrent remained constant and repeatable. This effect was attributed to an increase of the conductivity in the organic layers due a photo-

induced trap filling mechanism. It was demonstrated that the dark current tended to behave and to show the same dependences than the photocurrent after exposure to light.

Some donor-acceptor systems were investigated in lateral OPDs for deep ultraviolet detection (i.e. range of wavelengths below 320nm). It was shown that, with a proper choice of materials and configuration, lateral OPDs displayed peaks of efficiency at short wavelengths (270nm and 280nm) but suffered from lower detectivities compared to vertical architectures which was attributed to a poor collection efficiency.

Finally, the use of a phosphorescent sensitizer doped in the absorbing bottom layer of top-contact lateral OPDs was explored to improve their absorption efficiency. It is found that an effective energy-transfer pathway is possible in NPB:FIrpic and NPB:$Ir(ppy)_3$ mixtures is possible to generate long life and long diffusion length NPB triplet excitons. However, lateral OPDs with a doped absorbing layer showed lower photo-currents in comparison to standard structures. The effect of charge trapping near the donor-acceptor interface due to introduction of impurities was discussed.

8.2. Recommendations and future work

8.2.1. *Improvement of lateral OPDs performances*

It has been shown in this thesis that lateral OPDs suffer from low photocurrents. One way to increase the efficiency of lateral OPDs would be to increase the photogeneration of carriers by improving the absorption in the active layers. One way of improvement of top-contact lateral OPDs under bottom illumination would be to insert a top metallic cap to induce back reflection and re-absorption of light in the channel area which has been found to be the main photo-active area. In the case of top illumination a

reflective metal layer could be first deposited onto the substrate before the deposition of the organic layers.

8.2.2. *Development of lateral bilayer OPDs with a dual-selectivity thanks to the illumination direction*

It has been shown that lateral OPDs can show photoresponse under both top and bottom illuminations since the channel is the major active area. By using an appropriate bilayer structure, a lateral OPD could be selective for two distinct spectral regions depending whether the device is top or bottom illuminated. The use of a quantum dots layers could be relevant due to their high absorption tunability and selectivity.

8.2.3. *Development of vertical deep UV-OPDs and test photo-degradation and the effect of introducing contact buffer layers on the stability*

We concluded that vertical OPDs demonstrated higher efficiency for DUV applications than lateral ones. Even though good results have been reported, DUV OPDs remain scarce due to the difficulty of elaborating transparent electrodes below 350nm. Developing vertical DUV OPDs with efficiencies comparable to Si-based ones would first involve to identify and develop 250-320nm-transparent bottom contacts on quartz substrates (metal oxides, thin metals, etc.). Efficient donor-acceptor combinations for maximum absorption and photoconduction in this spectral region have already been identified. Testing the photostability of these devices would be of great interest since never reported before in this range of wavelengths. Exploring approaches to increase the photo-stability, such as inserting contact buffer layers (molybdenum oxide, lithium fluoride, etc.), would also be relevant.

References

[1] C. W. Tang and S. A. VanSlyke, *Appl. Phys. Lett.* ***51,*** *913(1987).*

[2] J. H. Burroughes, D. D. C. Bradley, A. R. Brown, R. N. Marks, R. H. Friend, P. L. Burn, and A. B. Holmes, *Nature (London)* ***347,*** *539(1990).*

[3] R. H. Friend, R. W. Gymer, A. B. Holmes, J. H. Burroughes, R. N. Marks, C. Taliani, D. D. C. Bradley, D. A. dos Santos, J. L. Bredas, M. Logdlund, and W. R. Salaneck, *Nature (London)* ***397,*** *121(1999).*

[4] U. Mitschke and P. Bauerle, *J. Mater.Chem.* ***10****, 1471(200).*

[5] Z. Bao, A. Dodalapur, and A.J. Loving, *Appl. Phys. Lett.* ***69****, 4108(1996).*

[6] H. E. Katz, *J. Mater. Chem.* ***7,*** *369(1997).*

[7] S. F. Nelson, Y. Y. Lin, D. J. GunYdlach, and T. N. Jackson, *Appl. Phys.Lett.* ***72,*** *1854(1998).*

[8] G. H. Gelinck, T. C. T. Geuns, and D. M. de Leeuw, *Appl. Phys. Lett* ***77,****1487(2000).*

[9] V.C. Sundar, J. Zaumseil, V. Podzorov, E. Menard, R.L. Willett, T. Someya, M.E. Gershenson, and J.A. Rogers, *Science* ***303****, 1644 (2004).*

[10] D. Wohrle and D.Meissner, *Adv. Mater. 3.129(1991).*

[11] P.Peumans, A.Yakimov, and S.R. Forrest, *J.Appl.Phys.* ***93****, 3693(2003).*

[12] J.G.Xue, S.Uchida, B.P. Rand, and S.R. Forrest, *Appl. Phys. Lett.* ***84****, 3013(2004).*

[13] http://www.sciencedaily.com/releases/2008/02/080206154631.htm *(accessed in July 2013).*

[14] http://www.theverge.com/2013/1/9/3855960/samsung-flexible-oled-phone-prototype-hands-on (*accessed in July 2103).*

[15] http://www.wired.com/gadgetlab/2009/03/displaysearch-s/ *(accessed in July 2013).*

[16] http://www.ubergizmo.com/2012/05/lg-55em600-55-inch-oled-tv/ *(accessed in July 2013).*

[17] http://arstechnica.com/science/2012/06/new-oled-lighting-panel-hopes-to-outshine-fluorescent-bulbs/ *(accessed in July 2013).*

[18] Organic Chemistry, G.M. Loudon, *The Benjamin/Cummings Publishing Company, Inc, 3rd ed.*

[19] Molecular Electronics, G. G. Ashwell, *Research Studies Press Ltd*, 1992.

[20] Chemistry and Physics of Modern Materials, Cowie.

[21] Degradation in Anthracene-based Organic Light Emitting Devices, Q. Wang, 2010.

[22] Organic Photoreceptors for Xerography, M. Borsenberger and D. S. Weiss, *Dekker, New York*, 1998.

[23] P. Rand, J. Genoe, P. Heremans, and J. Poortmans, *Prog. Photovoltaics* ***15****, 659 (2007)*.

[24] Peumans, A. Yakimov, and S. R. Forrest, *J. Appl. Phys.* ***93,*** *3693 (2003).*

[25] Illustration taken from *http://sciencefair.math.iit.edu/techniques/spectrophotometer/.*

[26] Principles of Photochemistry, Barltrop and Goyle, John Wiley and Sons, 1978.

[27] W. Y. Liang 1970 Phys. Educ. 5 226.

[28] Electronic Processes in Organic Crystals and Polymers, M. Pope and C. Swenberg, *Oxford Science Publications, 2nd ed*. 1999.

[29] C. Madigan and V. Bulovic, *Phys, Rev. Lett.* ***96****, 046404 (2006).*

[30] I. G. Hill, D. Milliron, J. Schwartz, and A. Kahn, *Appl. Surf. Sci.****166****, 354 (2000).*

[31] S. R. Forrest, *Chem. Rev. Washington, D.C.* ***97****, 1793 (1997).*

[32] B. P. Rand, D. P. Burk, S. R. Forrest, *Phys. Rev. B* ***75****, 115327 (2007).*

[33] Israel Institue of Technology-Technion, Electrical Engineering Course Material from http://webee.technion.ac.il/orgelect/excitons.pdf.

[34] Physics of Organic Semiconductors, W. Brutting, *Wiley-VCH,* 2005.

[35] H. Choukri, A. Fischer, S. Forget, S. Chénais, M-C. Castex, D. Adès, A. Siove, and B. Geffroy, *Appl. Phys. Lett.* ***89****, 183513 (2006).*

[36] N. S. Sariciftci, L. Smilowitz, A. J. Heeger, and F. Wudl, *Science* ***258****, 1474 (1992).*

[37] N. S. Sariciftci, D. Braun, C. Zhang, V. I. Srdanov, and A. J. Heeger, *Appl. Phys. Lett.* ***62****, 585 (1993).*

[38] C. H. Lee, G. Yu, D. Moses, K. Pakbaz, C. Zhang, N. S. Sariciftci, A. J. Heeger, and F. Wudl, *Phys. Rev. B.* ***48*** *(1993) 15425.*

[39] G. Yu, C. Zhang, and A. J. Heeger, *Appl. Phys. Lett.* ***64****, 1540 (1994).*

[40] G. Yu, J. Gao, J. C. Hummelen, F. Wudl, and A. J. Heeger*, Science* ***270*** *(1995) 1789.*

[41] G. Yu and A. J. Heeger *J. Appl. Phys.* ***78****, 4510 (1995).*

[42] J.J.M. Halls, C.A. Walsh, N.C. Greenham, E.A. Marseglia, R.H. Friend, SC. Moratti and A.B. Holmes, *Nature* ***376*** *(1995) 498.*

[43] Youngkyoo Kim, Stelios A. Choulis, Jenny Nelson, Donal D. C. Bradley, Steffan Cook et al., *Appl. Phys. Lett.* ***86****, 063502 (2005).*

[44] Valentin D. Mihailetchi, Hangxing Xie, Bert de Boer, Lacramioara M. Popescu, Jan C. Hummelen et al., *Appl. Phys. Lett.* ***89****, 012107 (2006).*

[45] D. Chirvase, J. Parisi, J. C. Hummelen, and V. Dyakonov*, Nanotechnology* ***15****, 1317–1323 (2004).*

[46] Y. Zhao, Z. Xie, Y. Qu, Y. Geng, and L. Wang, *Appl. Phys. Lett.* ***90****, 043504 (2007*).

[47] P. Peumans, V. Bulović, and S. R. Forrest, *Appl. Phys. Lett.* ***76****, 3855 (2000)*.

[48] J. Cabanillas–Gonzalez , O, Peña–Rodríguez , I. Suarez Lopez , M. Schmidt , M. I. Alonso et al., *Appl. Phys. Lett.* ***99****, 103305 (2011)*.

[49] X. Gong, M. Tong, Y. Xia, W. Cai, J. S. Moon, Y. Cao,G. Yu, C-L. Shieh, B. Nilsson, and A. J. Heeger, *Science* ***325****, 1665 (2009)*.

[50] S-H. Wu, W-L. Li, B. Chu, Z-S. Su, F. Zhang et al., *Appl. Phys. Lett.* ***99****, 023305 (2011)*.

[51] D. Natali, M. Sampietro, M. Arca, C. Denotti, and F. A. Devillanova, *ESSDERC 2002*.

[52] J. C. Ho, A. Arango , and V. Bulović, *Appl. Phys. Lett.* ***93****, 063305 (2008)*.

[53] M. Caironi , T. Agostinelli , D. Natali , M. Sampietro , R. Cugola et al., *J. Appl. Phys.* ***102****, 024503 (2007*).

[54] T. P. Osedach, S. M. Geyer, J. C. Ho, A. C. Arango, M. G. Bawendi, and V. Bulović, *Appl. Phys. Lett.* ***94,*** *043307 (2009)*.

[55] T. P. Osedach, N. Zhao, S. M. Geyer, L-Y. Chang, D. D. Wanger,

A. C. Arango, M. C. Bawendi, and V. Bulovic, *Adv. Mater,* ***22,*** *5250–5254, (2010)*.

[56] U. Shafique, K. S. Karim, *Proc. of SPIE Vol. 7961 796103-1*.

[57] I. Khodami, F. Taghinakhsh, and K. S. Karim, *IEEE Electron. Device Lett.,* ***29****, 1007 (2008)*.

[58] I-m. Chan, F. C-N. Hong, *Thin Solid Films 444 (2003) 254–259*.

[59] Q. L. Song, C. M. Li Mary B. Chan-Park, M. Lu, H. Yang, and X.Y. Hou, *PRL* ***98****, 176403 (2007)*.

[60] K. Wang, F. Chen, K-W Shin, N. Allec, and K. S. Karim, *Proc. of SPIE, 7622, 762217 (2010).*

[61] A. Foertig, A. Wagenpfahl, T. Gerbich, D. Cheyns, V. Dyakonov, and C. Deibel, *Adv. Energy Mater.* ***2012****, 2, 1483–1489.*

[62] H. Choukri, A. Fischer, S. Forget, S. Chénais, M-C. Castex, D. Adès, A. Siove, and B. Geffroy, *Appl. Phys. Lett.* ***89****, 183513 (2006).*

[63] S. Naka, H. Okada, H. Onnagawa, T. Tsutsui, *Appl. Phys. Lett.* ***76*** *(2000) 197.*

[64] H. H. Fong, Wallace C. H. Choy, K. N. Hui, and Y. J. Liang, *Appl. Phys. Lett.* ***88****, 113510 (2006).*

[65] W.C.H. Choy, K.N. Hui, H.H. Fong, Y.J. Liang, P.C. Chui, *Thin Solid Films 509 (2006) 193– 196.*

[66] Satoshi Ogawa, Tatsuo Naijo, Yasuo Kimura, Hisao Ishii, and Michio Niwano, *Appl. Phys. Lett.* ***86****, 252104 (2005).*

[67] L. Zhu, Q. Dai, Z-F. Hu, X-Q. Zhang, and Y-S. Wang, *IEEE Photonic Technology Letters,* ***Vol. 23****, No. 23, December 1 (2011).*

[68] L. Zhu, Q. Dai, Z-F. Hu, X-Q. Zhang, and Y-S. Wang, *Optics Letters, Vol.* ***36****, No. 10, May 15 (2011).*

[69] S-H. Wu, W-L. Li, B. Chu, C. S. Lee, Z-S. Su et al. *Appl. Phys. Lett.* ***96****, 093302 (2010).*

[70] J. U. Wallace, R. H. Young, C. W. Tang, and S. H. Chen, *Appl. Phys. Lett.* ***91****, 152104 (2007).*

[71] S. T. Roberts, C. W. Schlenker, V. Barlier, R. E. McAnally, Y. Zhang, J. N. Mastron, M. E. Thompson, and S. E. Bradforth, *J. Phys. Chem. Lett. 2011, 2, 48–54.*